Defying jet-gas alignment in two radio galaxies at z 2 with extended light profiles: Similarities to brightest cluster galaxies

C. Collet, N. P. H. Nesvadba, C. De Breuck, M. D. Lehnert, P. Best, J. J. Bryant, D. Dicken, H. Johnston, R. Hunstead, D. Wylezalek

A&A 579, A89 (2015)
DOI: 10.1051/0004-6361/201424544

Astronomy & Astrophysics

Defying jet-gas alignment in two radio galaxies at $z \sim 2$ with extended light profiles: Similarities to brightest cluster galaxies⋆,⋆⋆

C. Collet[1], N. P. H. Nesvadba[1], C. De Breuck[2], M. D. Lehnert[3], P. Best[4], J. J. Bryant[5,6,7], D. Dicken[1,8], H. Johnston[5], R. Hunstead[5], and D. Wylezalek[2,9]

[1] Institut d'Astrophysique Spatiale, CNRS, Centre Universitaire d'Orsay, Bat. 120-121, 91405 Orsay, France
e-mail: nicole.nesvadba@ias.u-psud.fr
[2] European Southern Observatory, Karl-Schwarzschild Strasse, 85748 Garching bei München, Germany
[3] Institut d'Astrophysique de Paris, UMR 7095 CNRS, Université Pierre et Marie Curie, 98 bis boulevard Arago, 75014 Paris, France
[4] SUPA, Institute for Astronomy, Royal Observatory of Edinburgh, Blackford Hill, Edinburgh EH9 3HJ, UK
[5] Sydney Institute for Astronomy (SIfA), School of Physics, The University of Sydney, Sydney, NSW 2006, Australia
[6] Australian Astronomical Observatory, PO Box 915, North Ryde, NSW1670, Australia
[7] ARC Centre of Excellence for All-sky Astrophysics (CAASTRO), Australia
[8] Laboratoire AIM Paris-Saclay, CEA/DSM/Irfu, Orme des Merisiers, Bat 709, 91191 Gif sur Yvette, France
[9] Department of Physics and Astronomy, Johns Hopkins University, 3400 N. Charles St, Baltimore, MD 21218, USA

Received 7 July 2014 / Accepted 5 March 2015

ABSTRACT

We report the detection of extended warm ionized gas in two powerful high-redshift radio galaxies, NVSS J210626-314003 at $z = 2.10$ and TXS 2353-003 at $z = 1.49$, that does not appear to be associated with the radio jets. This is contrary to what would be expected from the alignment effect, a characteristic feature of distant, powerful radio galaxies at $z \geq 0.6$. The gas also has smaller velocity gradients and line widths than most other high-z radio galaxies with similar data. Both galaxies are part of a systematic study of 50 high-redshift radio galaxies with SINFONI, and are the only two that are characterized by the presence of high surface-brightness gas not associated with the jet axis and by the absence of such gas aligned with the jet. Both galaxies are spatially resolved with ISAAC broadband imaging covering the rest-frame R band, and have extended wings that cannot be attributed to line contamination. We argue that the gas and stellar properties of these galaxies are more akin to gas-rich brightest cluster galaxies in cool-core clusters than the general population of high-redshift radio galaxies at $z \gtrsim 2$. In support of this interpretation, one of our sources, TXS 2353-003, for which we have Hα narrowband imaging, is associated with an overdensity of candidate Hα emitters by a factor of ∼8 relative to the field at $z = 1.5$. We discuss possible scenarios of the evolutionary state of these galaxies and the nature of their emission line gas within the context of cyclical AGN feedback.

Key words. Galaxy: formation – galaxies: active – quasars: emission lines – galaxies: high-redshift – galaxies: clusters: general – galaxies: jets

1. Introduction

Powerful radio galaxies at redshifts $z \geq 1{-}2$ (HzRGs) are particularly massive (several 10^{11} $M_\odot$, e.g., Seymour et al. 2007; De Breuck et al. 2010), intensely star-forming (on the order of 1000 $M_\odot$ yr^{-1}; Archibald et al. 2001; Reuland et al. 2004; Seymour et al. 2012; Ivison et al. 2012; Barthel et al. 2012; Drouart et al. 2014), relatively evolved (Nesvadba et al. 2011a) galaxies. Many are surrounded by overdensities of satellite galaxies, making them interesting tracers of overdense regions in the early Universe that may ultimately evolve into massive, rich galaxy clusters (e.g., Chambers et al. 1996; Le Fevre et al. 1996; Kurk et al. 2004a; Venemans et al. 2007; Galametz et al. 2012; Wylezalek et al. 2013). Their co-moving number density corresponds to that of massive clusters, when corrected for duty-cycle effects (Venemans et al. 2007; Nesvadba et al. 2008). Particularly detailed studies of individual HzRGs suggest that at least one subset of this population could be the progenitors of the central galaxies in massive clusters in the nearby Universe (e.g., Hatch et al. 2009). They follow the low-redshift Kormendy relation of powerful radio and brightest cluster galaxies when allowing for passive luminosity evolution (Targett et al. 2011). Many HzRGs are themselves gas rich (e.g., van Ojik et al. 1997; Nesvadba et al. 2008; Ogle et al. 2012; Emonts et al. 2014), and while they have no well established, virialized halos of hot gas (Overzier et al. 2005), HzRGs do have extended (few 100 kpc) reservoirs of diffuse warm ionized gas (Villar-Martín et al. 2003) with embedded clouds or filaments of neutral (van Ojik et al. 1997; Adams et al. 2009) and molecular gas (Nesvadba et al. 2009; De Breuck et al. 2003; Emonts et al. 2014). As suggested by, e.g., Villar-Martín et al. (2003) these could be the vestiges of the gaseous reservoirs from which the brightest cluster and other galaxies formed.

The central, high surface-brightness regions of HzRGs are well fitted with de Vaucouleurs profiles with relatively large

⋆ Based on observations carried out with the Very Large Telescope of ESO under Program IDs 079.A-0617, 084.A-0324, 085.A-0897, and 090.A-0614.

⋆⋆ Appendix A is available in electronic form at http://www.aanda.org

radii, $R \sim 8$ kpc (Targett et al. 2011), but extended, often irregular line and continuum emission in HzRGs is found preferentially along the radio jet axis (e.g., Cimatti et al. 1993). The reasons for this alignment effect are still not fully understood. Polarimetry suggests that light scattering on dust grains could be the origin of at least some of the extended continuum light; other authors favor jet-triggered star formation (Chambers et al. 1988; Klamer et al. 2005) as the cause of the extended continuum emission.

The kinematics in the extended gas around HzRGs are often strongly perturbed (e.g., Baum & McCarthy 2000; Villar-Martín et al. 2003). SINFONI imaging spectroscopy showed this is the case in individual regions of these galaxies, and throughout their extended emission-line gas (Nesvadba et al. 2006, 2008). Warm ionized gas seems to be a major component of the interstellar meduim (ISM) in these galaxies, with ionized gas masses of up to $\gtrsim 10^{10}$ $M_\odot$ in some cases (Nesvadba et al. 2008, 2006), comparable to the molecular gas masses found in some HzRGs (e.g., Emonts et al. 2014; Nesvadba et al. 2009; De Breuck et al. 2005). Broad line widths and abrupt velocity offsets of up to 2000 km s^{-1} found in this gas are not reconcilable with gravitational motion. Instead they suggest that a small part of the kinetic energy release from the active galactic nucleus (AGN), through powerful radio jets, accelerates large fractions of the ISM in these galaxies to velocities well above the escape velocity from the underlying dark-matter halo, thereby driving winds and removing the fuel for subsequent star formation. This scenario is broadly supported by hydrodynamic models showing that jets may indeed accelerate relatively dense gas to observed velocities of several 100 km s^{-1} (Wagner et al. 2012).

Using VLT near-infrared imaging spectroscopy we have carried out a large survey of the rest-frame optical line emission of the warm ionized gas in a set of 50 radio-selected HzRGs at $z \gtrsim 2$ spanning three orders of magnitude in radio power from a few times 10^{26} to a few times 10^{29} W Hz^{-1} at 1.4 GHz in the rest frame, and more than two orders of magnitude in radio size, from 1 kpc to about 300 kpc (Collet et al., in prep.; Nesvadba et al., in prep.). Emission-line regions are well aligned with the radio jet axis in all but two galaxies with extended line emission, which in addition to kinematic, energy, and timing arguments suggests that this gas represents outflows of warm ionized gas driven by the overpressurized cocoon of hot plasma inflated by the radio source. These galaxies are described in greater detail in Nesvadba et al. (2006), Nesvadba et al. (2007), Nesvadba et al. (2008), Nesvadba et al. (2011a) and Collet et al. (in prep.).

Here we discuss the two radio galaxies, TXS 2353−003 and NVSS J210626−314003, that do not follow these global trends. Their extended regions of warm ionized gas with similar surface brightness to the other sources show strong offsets in position angle to the radio jet axis, contrary to what is expected from the alignment effect and observed in the other galaxies within the SINFONI sample. Gas associated with the radio jet axis, if present at all, is not a distinctive component compared to gas along other directions in our SINFONI data. Gas that is seen in projection to be associated with the jet axis may or may not imply a physical association; however, it is clear that gas that is globally and significantly offset from the jet axis as projected on the sky is not reconcilable with a scenario where the gas is embedded in an overpressured cocoon inflated by the on-going jet activity. In addition, the line widths are low compared to the rest of our sample. Line widths near the nucleus are higher, and may be affected by the central radio source.

TXS 2353-003 and NVSS J210626-314003 are among the sources with the largest radio sizes in our sample, with largest angular sizes LAS = 38.8″ and 24.2″ at 4.86 GHz (De Breuck et al. 2001) and 2.368 GHz, respectively (corresponding to 310 kpc and 190 kpc at their redshifts of $z = 1.49$ and $z = 2.10$, respectively). Both have very regular centimeter radio morphologies (Collet et al., in prep.; Nesvadba et al., in prep.), and do not have bright radio cores. Both are associated with overdensities seen in projection along nearby lines of sight of distant ($z \geq 1.3$) IRAC sources in the CARLA survey of Wylezalek et al. (2013). TXS 2353-003 is within the densest region of their overall sample of 200 HzRGs. We highlight the similarities between our galaxies and brightest cluster galaxies at low redshift, including the extended emission-line gas, which resembles the warm ionized gas in and around the central galaxies of cool-core clusters in several respects.

We describe our SINFONI and ISAAC observations and data reduction in Sect. 2, and discuss the results of these observations in Sect. 3 for the line emission and in Sect. 4 for the continuum, where we also fit surface brightness profiles. In Sect. 5 we present our narrowband search for line emitters around TXS 2353-003 and argue that this galaxy is surrounded by an overdensity of line emitters, like many other HzRGs at somewhat greater redshifts. We compare these results with the IRAC results obtained as part of the CARLA survey (Wylezalek et al. 2013) in Sect. 6. In Sect. 7 we discuss several hypotheses regarding the nature of the emission-line regions in these two galaxies, which, given their strong misalignment relative to the jet axis, are unlikely to be directly associated with an expanding cocoon driving an outflow. We summarize our results in Sect. 8. Throughout our analysis we adopt a flat cosmology with $H_0 = 7$ km s^{-1} Mpc^{-1}, $\Omega_\Lambda = 0.7$, $\Omega_M = 0.3$. For NVSS J210626-314003 at $z = 2.1$, this corresponds to $D_L = 16.6$ Gpc, and for TXS 2353−003 at $z = 1.49$ to $D_L = 10.8$ Gpc, respectively; 1″ corresponds to 8.4 kpc for both galaxies.

2. Observations and data reduction

2.1. VLT/SINFONI imaging spectroscopy

We observed both galaxies with the near-infrared imaging spectrograph SINFONI on UT 4 of the Very Large Telescope (VLT) of ESO. The NVSS J210626-314003 data were taken on 2009 October 12, and those of TXS 2353-003 on 2010 August 13. The data were obtained as part of a comprehensive observational program to study the emission-line gas kinematics of 50 powerful radio galaxies at $z \geq 2$. We used the $H + K$ band covering a spectral range of 1.45−2.45 μm at a spectral resolving power $R = 1500$. The data were taken during good to moderate observing conditions, with a typical point spread function of 1″ × 1″ along right ascension and declination, dominated by the seeing. We used the 250 mas pixel scales with a field of view of 8″ × 8″, covering a field of 67 kpc × 67 kpc at $z = 2$.

Total integration times were 145 min for TXS 2353-003 and 120 min for NVSS J210626-314003, and were obtained in one-hour sequences of individual 300 s exposures. Our data reduction relied on a combination of IRAF and IDL routines (for details see, e.g., Nesvadba et al. 2011a,b). The absolute flux scale was measured by comparing our data with observations of standard stars with known magnitudes from the 2MASS survey that were observed at the end of each observing session. We also determined the size of the seeing disk from these stars.

2.2. VLT/ISAAC imaging

Both galaxies were also observed with ISAAC on UT 3 of the VLT between 2012 September 30 and 2012 October 2 through the service-mode program 090.A-0614. TXS 2353−003 was observed in the H band and through the narrowband FeII filter (NB 1.64) with $FWHM = 0.025$ μm (corresponding to a velocity range of $\Delta v = 4570$ km s^{-1}), so we cover Hα and [NII] at $z = 1.49$. NVSS J210626-314003 was only observed in the Ks band. Both broadband images cover roughly the rest-frame R band.

With the NB 1.64 filter we obtained a total of 248 minutes of on-source observing time of TXS 2353−003 split into 99 exposures with individual observing times of 150 s, and grouped into observing sequences of one hour each. After visual inspection we discarded 17 of these frames because of residuals from a strongly saturated star. The on-source observing time was thus 205 min.

In the H band we obtained 29 exposures for TXS 2353-003 with individual observing times of 72 s, corresponding to six detector readouts after 12 s. We discarded one frame which contained the trail of a satellite. In the K band for NVSS J210626−314003, we obtained 25 exposures of 90 s, corresponding to six detector readouts after 15 s. Total observing times in the H and K bands were therefore 35 min and 38 min for TXS 2353−003 and NVSS J210626−314003, respectively.

Data were dark-subtracted and flat-fielded, where we constructed the sky flats directly from the science data. All frames were then combined with the IRAF task `xdimsum`. Flux calibration relied on standard stars observed during the same night and at similar air mass to the science data. We used the Starlink GAIA software (Draper et al. 2014) to calculate the astrometry relative to 2MASS reaching rms = 0.07″ for TXS 2353−003, and rms = 0.3″ for NVSS J210626−314003, respectively. We also used 2MASS to verify our flux calibration, finding a good agreement within $\lesssim$10%. The sizes of stars in the image suggest the seeing was $FWHM = 0.5''$ in the H-band and NB 1.64 image of TXS 2353−003, and of $FWHM = 0.4''$ in the Ks-band image of NVSS J210626-314003. The limiting rms surface brightness in these images is 26.2 mag arcsec^{-2} and 23.6 mag arcsec^{-2} in the narrow and broadband image of TXS 2353−003, respectively. For the Ks-band image of NVSS J210626−314003, we find 23.7 mag arcsec^{-2}.

2.3. Narrowband observations of TXS 2353−003

To construct a continuum-subtracted line image from the narrowband image of TXS 2353-003, we approximate the underlying continuum in the narrowband filter by a scaled version of the flux measured through the broadband filter, taking into account the relative filter bandwidths of the narrow and broadband filters, and their transmission. Here we assume that the continuum is flat and uniform across the H-band filter.

We measured the zero points in the narrowband filter from standard stars. From the zero points in each filter, filter bandwidths, and transmissions of the narrow and broadband filters, we determine that the continuum flux density observed through the narrowband image corresponds to about 7.2% of the flux density measured through the broadband image. We would therefore need to scale the broadband image by this value before subtracting it from the narrowband image to obtain the flux density from the emission lines. When directly comparing the flux density of 12 stars in both images, we empirically find that a very similar scaling factor of 7.6% is best to minimize the residuals of the stellar continuum after the subtraction, and this is the factor that we used.

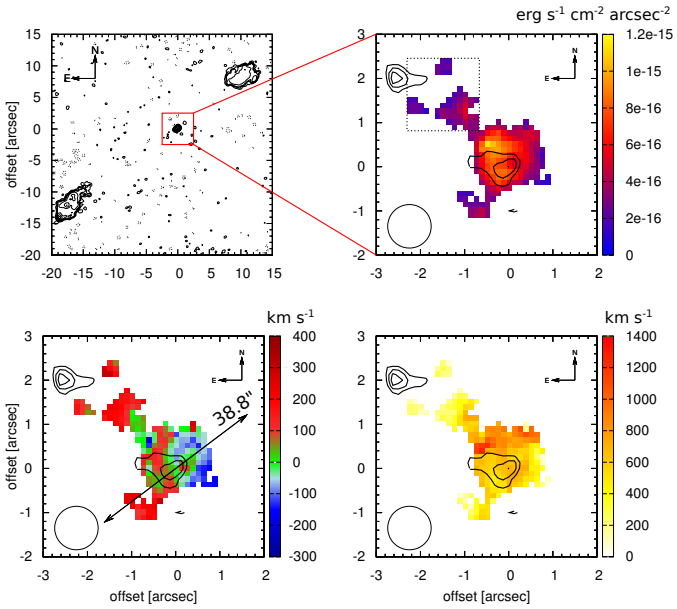

Fig. 1. Results of our observations of TXS 2353-003. *Top left*: 5.5 GHz contours from ATCA. *Clockwise from top right to bottom left*: SINFONI maps of [OIII]λ5007 surface brightness, FWHM line widths, and relative velocities. The square in the *top left panel* shows the size of the SINFONI maps compared to radio size. Black contours show the 5.5 GHz radio continuum, and the dotted square in the *top right panel* illustrates the region from which the bottom spectrum in Fig. 3 was extracted. The arrow in the *lower left panel* shows the direction of the radio jet, and the number gives the jet size in arcsec. Ellipses in the lower left corner of each panel show the FWHM size of the point spread function.

The redshifted wavelength of Hα in the radio galaxy is slightly blueshifted relative to the wavelength of peak throughput of the narrowband filter. Comparing this with the flux measured in the SINFONI data cube, and assuming that the relative flux calibration between both images is perfect, we find that we are missing between 20 and 25% of the line flux in the continuum-subtracted line image. For other Hα emitters (Sect. 5), for which we have no precise redshift estimates, we would first need to obtain spectroscopy before we can make similar corrections.

To evaluate the completeness limit of our data, we added faint artificial sources with the size of the seeing disk at sky positions in each frame of the narrow- and broadband images before re-reducing these data and extracting sources in the same way as for the final scientific analysis. We used fluxes between 2 and 11 times the rms in the central regions of the image. Adding the artificial sources to the individual frames rather than the final image helps to take misalignments between frames into account. We find that we recover 90% of sources with surface brightness above 1.5×10^{-19} erg s^{-1} cm^{-2} Å^{-1} arcsec^{-2} (or above 23.6 mag$_{\rm AB}$ arcsec^{-2}).

3. Imaging spectroscopy of the warm ionized gas

The SINFONI maps of NVSS J210626-314003 and TXS 2353-003 are shown in Figs. 1 and 2, respectively. In NVSS J210626−314003 at $z = 2.104$, [OIII]$\lambda\lambda$4959, 5007

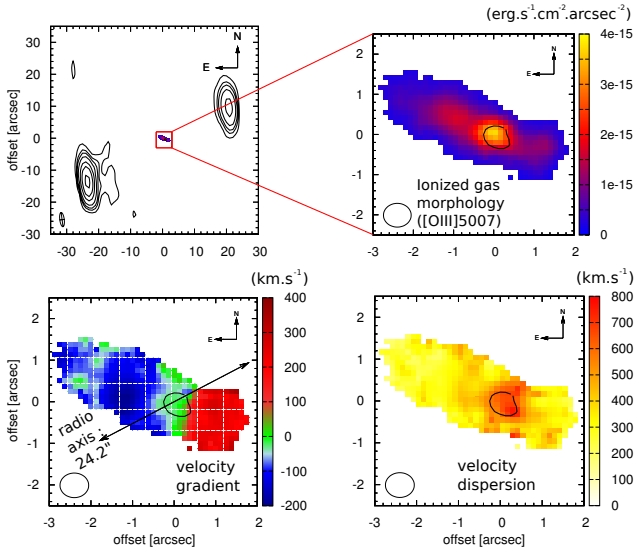

Fig. 2. Results of our observations of NVSS J210626−314003. *Top left*: 5.5 GHz contours from ATCA. *Clockwise from top right to bottom left:* SINFONI maps of [OIII]λ5007 surface brightness, FWHM line widths, and relative velocities. The square in the *top left* shows the size of the SINFONI maps compared to radio size. The black contour marks the continuum position in our SINFONI cube. Ellipses in the lower left corner of each panel show the FWHM size of the point spread function.

and Hβ fall into the *H* band, and Hα, [NII]$\lambda\lambda$6548, 6583, and [SII]$\lambda\lambda$6716, 6731 fall into the *K* band, both of which we cover with our data cubes. In TXS 2353−003, we identify Hα and [NII]$\lambda\lambda$6548, 6583 at wavelengths corresponding to a redshift of $z = 1.49$. At this redshift, [OIII]$\lambda\lambda$4959, 5007 and Hβ fall at redshifts below the lower wavelength cutoff of our grating, $\lambda_{\rm min} = 1.45\,\mu$m.

Our redshift measurement for TXS 2353-003 does not agree with the previous redshift of $z = 2.59$ measured with longslit spectroscopy, which was thought to have detected Lyα in the observed optical wavelength range (De Breuck et al. 2001), but was in hindsight probably affected by a Cosmic ray. We did not identify any possible emission line consistent with the previous redshift $z = 2.59$, although [OIII]$\lambda\lambda$4959, 5007 and Hβ should fall into the *H* band, and [NII]$\lambda\lambda$6548, 6583, and Hα should fall into the *K* band at that redshift. The rest-frame UV spectrum shows no other line candidate consistent with $z = 2.59$; the value for Lyα at the redshift $z = 1.49$ we measure here falls well below the UV atmospheric cutoff.

Both galaxies have bright, spatially well-resolved line emission. We fitted the extended line emission in both galaxies with single Gaussian profiles. Spectra were extracted from small apertures of $0.4'' \times 0.4''$, which helps to reduce the strongest pixel-to-pixel noise while safely oversampling the seeing disk so that no spatial information is lost. The data were also smoothed in the spectral direction by three pixels, without loss of spectral resolution. Our fitting routine interpolates over wavelength ranges dominated by bright night-sky line residuals, and we only map spatial pixels where a line was detected at a $S/N > 3$.

Line emission extends beyond the bright continuum seen in the SINFONI cubes (but not in the ISAAC broadband image which we will discuss later in more detail and show in Figs. 7 and 8, which is deeper in the continuum). The sizes of the extended emission-line regions of NVSS J210626-314003 and TXS 2353−003 are $5.3'' \times 2.0''$ (44 kpc × 17 kpc) and $2.5'' \times 2.0''$ (21 kpc × 17 kpc) along the major and minor axis, respectively, and down to surface-brightness limits of 4.3×10^{-17} erg s^{-1} cm^{-2} arcsec^{-2} and 6.2×10^{-17} erg s^{-1} cm^{-2} arcsec^{-2}.

In NVSS J210626−314003 the emission-line region is roughly centered on the continuum peak. In TXS 2353−003, the gas appears more lopsided. This is also seen in the continuum-subtracted ISAAC narrowband image (source "a" in Fig. A.1). The morphology of the ionized gas in both observations is fairly consistent: a bright emission-line region associated with the radio galaxy, more extended toward the southeast and northwest. The integrated spectrum extracted from this fainter region, shown as a dashed region in Fig. 1, clearly shows Hα and [NII]λ6583 (Fig. 3). Fluxes and other line properties are listed for both galaxies in Table 1. In TXS 2353−003, we note a faint continuum emitter along the direction of extended gas, but at a larger distance. In NVSS J210626−314003 no further continuum source is observed along the major axis of the emission-line region.

In the SINFONI cube, NVSS 210626-3134003 shows a smooth velocity gradient of about 600 km s^{-1} over 25 kpc. In TXS 2353−003 we observe a more irregular velocity pattern, which could be at least in part due to the lower signal-to-noise ratio and irregular line profiles. In NVSS J210626-3134003, where we observe [OIII]λ5007 and Hα at good signal-to-noise ratios, the gas kinematics and morphologies are similar in both lines.

Both galaxies have broad line widths with $FWHM \sim 800$ km s^{-1} around the continuum peak which we associate with the central regions of the galaxies. These lines are broader than those of star-forming galaxies at similar redshifts, including the most massive, intensely star-forming dusty galaxies such as sub-millimeter galaxies (e.g., Swinbank et al. 2006), and are consistent with those found in other powerful radio galaxies at similar redshifts (e.g. Nesvadba et al. 2008; Collet et al., in prep.). Following the arguments given in these studies, we consider the broad line widths as evidence that the gas in the central regions of our sources is stirred up by the transfer of kinetic energy from the radio source.

The gas kinematics at larger radii are more quiescent in both sources. Line widths in the extended gas of NVSS J210626-314003 and TXS 2353-003 are $FWHM = 300$–400 km s^{-1} (Figs. 1 and 2), more akin to those observed in a quasar illumination cone at $z \sim 2$ (Lehnert et al. 2009) and Lyα blobs without a powerful central radio source (e.g., Wilman et al. 2005; Overzier et al. 2013), than to powerful radio galaxies, including the central regions of our two sources here.

A marked difference to other HzRGs with similar data is that most of the emitting gas is at large position angles from the radio jet axis. Typically, the jet axis and the semi-major axis of the gas are aligned within about 20°–30° (Fig. 4, see also Collet et al., in prep.; Nesvadba et al., in prep.). Given the size of the minor axis of the extended line emission of up to ∼15–20 kpc and beam smearing effects in the radio and near-infrared, this range is on the order of what would be expected if gas and jet were associated with each other, for example, if the jet inflated a hot bubble of overpressurized gas like in the cocoon model (Begelman & Cioffi 1989). In NVSS J210626−314003 and TXS 2353−003, however, the relative position angle between extended gas and radio jet axis is much larger, 60° and 90°, respectively, and the jet is not embedded within the emission line gas, as expected from a cocoon inflated by the jet. Figure 4 shows that both

Table 1. Properties of the two galaxies discussed in this study.

	TXS 2353−003	NVSS J210626−314003
Redshift	1.487	2.104
D_L [Gpc]	10.8	16.6
Radio power [10^{28} W Hz^{-1}]	3.7	4.2
Radio size [arcsec]	38.8	24.2
Radio size [kpc]	328	201
K-band magnitude [mag]	18.1 ± 0.3	18.7 ± 0.2
PA offset between jet and gas	∼90°	∼60°
F([OIII]λ5007)^a	...	66 ± 13
F(Hβ)^a	...	5.2 ± 1
F([NII]λ6548)^a	2.8 ± 0.6	1.2 ± 0.2
F([NII]λ6583)^a	8.3 ± 1.7	3.7 ± 0.7
F([SII]λ6716)^{a,b}	1.4 ± 0.5	2.3 ± 0.5
F([SII]λ6731)^a	4.1 ± 1.0	2.2 ± 0.5
F(Hα)^a	12.0 ± 2.4	14.7 ± 3.0
$\mathcal{L}$(Hα) [10^{43} erg s^{-1}]	1.7	4.8
Ionized gas mass [10^8 $M_\odot$]	2.4	9.3
SINFONI rms^c	4.3	6.2

Notes. $^{(a)}$ All fluxes are given in units of 10^{-16} erg s^{-1} cm^{-2}. $^{(b)}$ [SII]λ6716 in TXS 2353−003 is affected by a telluric line. $^{(c)}$ Surface brightness detection limit in units of 10^{-17}erg s^{-1} cm^{-2} arcsec^{-2}.

galaxies clearly stand out from the overall sample of HzRGs with SINFONI observations.

3.1. Line diagnostics

The ratios of bright optical line emission provide important constraints on the ionizing source and other gas properties in the extended emission-line regions of galaxies (Baldwin et al. 1981; Veilleux & Osterbrock 1987; Kewley et al. 2006). Collet et al. (in prep.) discussed the emission-line ratios of NVSS J2106-314003 in the context of their overall sample of moderately powerful HzRGs, finding [NII]/Hα and [OIII]/Hβ ratios that correspond to neither the classical starburst nor the AGN branch. In TXS 2353-003, we only have [NII] and Hα measured with a fairly high ratio of [NII]/Hα = 0.7 in the extended gas (Fig. 3), which alone is sufficient to safely attribute the line emission to either shocks or photoionization from the AGN (Fig. 5). Off-axis gas not aligned with the radio jet axis and out to a galactocentric radius of 65 kpc in the radio galaxy 3C 265 at z = 0.8 may indeed be powered by shocks, perhaps with additional photoionization from soft X-ray emission from the precursor of the shock (Solórzano-Iñarrea et al. 2002). However, as argued by Le Tiran et al. (2011) and Nesvadba et al. (2006), it is difficult to reach high Hα surface brightnesses as observed with shocks. The same is the case for shock-heated, likely infalling clouds in the cluster central galaxy NGC 4696 (Farage et al. 2010).

Like TXS 2353-003, NVSS J210626-314003 also falls outside the star formation branch; however, it also falls outside the sequence formed by low-redshift AGN in the SDSS. The line ratios are consistent with low-metallicity gas photoionized by an AGN, as expected in the models of Groves et al. (2006) and Kewley et al. (2013), and as shown with the solid blue lines in Fig. 5. These lines show the range of line ratios expected for galaxies at z = 1.5 with intense star formation typical for galaxies at these redshifts, and AGN with metal-poor narrow line regions and a metal enrichment history predicted by cosmological models of galaxy evolution (Davé et al. 2011). These conditions are referred to as "model 4" by Kewley et al. (2013). J-band spectroscopy would be required to investigate whether TXS 2355-003 falls onto the low-redshift AGN branch or above.

4. Continuum morphologies

4.1. Line-free continuum images from SINFONI

We also constructed line-free continuum images from our SINFONI cubes (shown as contours in Figs. 1 and 2) for both galaxies by collapsing the data cubes along the spectral direction over all wavelengths that are free from emission lines and prominent night-sky line residuals. We consider the continuum peak in the cube to be the location of the galaxy nucleus, which may be dominated either by stellar light or the AGN. At a projected distance of about 3″ (24 kpc) northeast of TXS 2353-003, we find another, fainter H-band source. We do not detect any line emission from this galaxy, so we cannot determine whether it is physically associated with the radio galaxy, or an interloper along the line of sight. NVSS J210626−314003 appears to be an isolated source, except for two much fainter sources at 1.7″ and 3.9″ toward the southeast (corresponding to projected separations of 14.3 kpc and 32.8 kpc at z = 2.1, respectively), which however are not aligned with the extended emission-line regions. We do not detect any line emission from the nearer source, and the more distant source falls outside the field of view of SINFONI. It is therefore not clear if they are associated with the radio galaxy. For TXS 2353-003, for which we do not have broadband K-band imaging, we measure a K-band magnitude of 18.1 ± 0.2 mag from our SINFONI data cube within a 3″ aperture.

4.2. ISAAC broadband imaging

In Figs. 7 and 8, we have already shown the rest-frame R-band morphologies of TXS 2353−003 and NVSS J210626-314003 observed in the H and Ks band, respectively. Both galaxies are clearly spatially resolved, even with ground-based, seeing-limited images. This is best seen in Fig. 6 which shows the azimuthally averaged surface-brightness profiles of both sources compared to the profiles of nearby stars taken from the same images, showing a clear excess of continuum emission out to large radii in both galaxies.

Both galaxies have a bright central region (which is more regular in NVSS J210626-314003 than in TXS 2353−003)

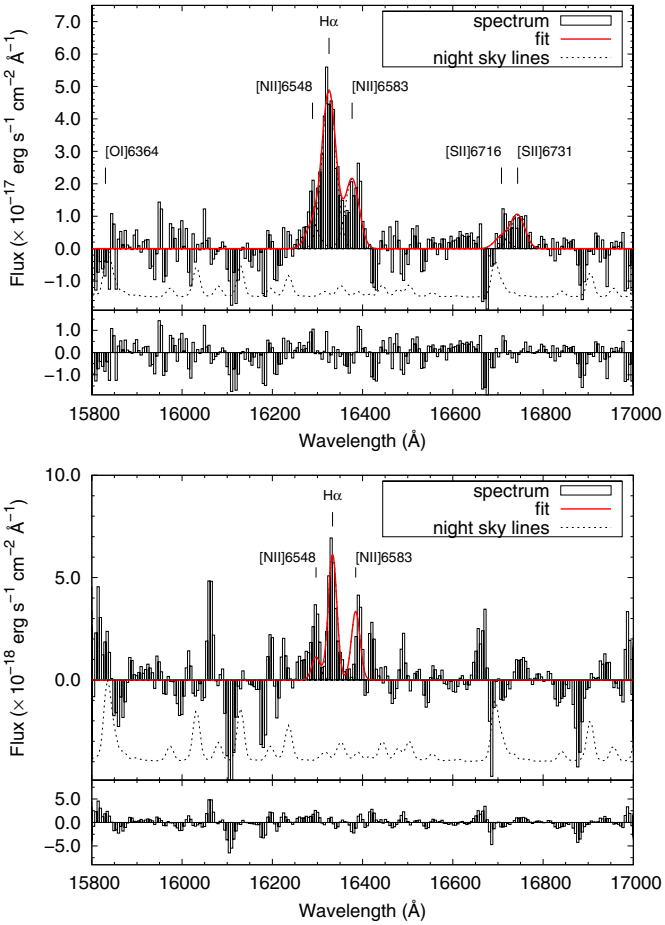

Fig. 3. *Top*: spectrum of TXS 2353−003, integrated over all spatial pixels where the Hα emission from the galaxy is detected at $\geq 3\sigma$, and corrected for velocity shifts. *Bottom*: integrated spectrum of the north-eastern part of the emission-line region of TXS 2353−003, defined by the dotted square in Fig. 1.

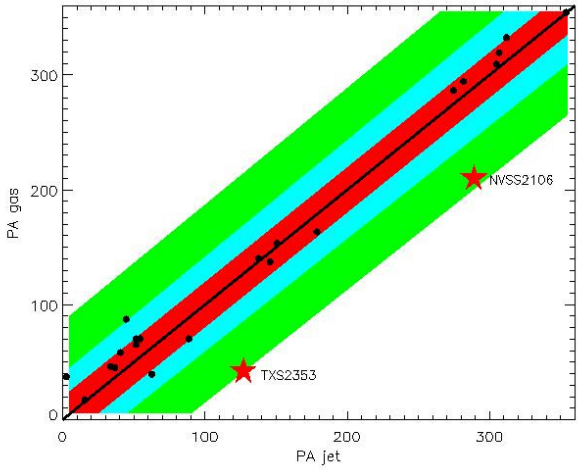

Fig. 4. Position angle (north through east) of the gas (ordinate) as a function of the position angle of the radio jet for our two sources. The outer boundaries of the red, blue, and green stripes indicate offsets of 20°, 45°, and 90°, respectively. Red stars indicate our two sources discussed here, small black dots show the remaining HzRGs with SINFONI data and well-determined position angles (Nesvadba et al., in prep.).

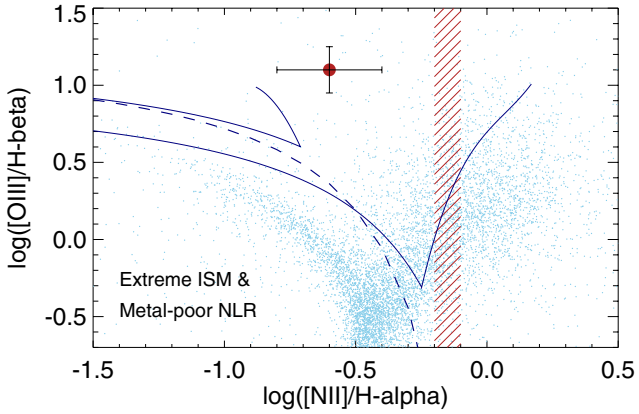

Fig. 5. Diagnostic diagram showing the ratio of [OIII]/Hβ as a function of [NII]/Hα line ratio (Baldwin et al. 1981; Veilleux & Osterbrock 1987). The red dot shows the position of NVSS J210626-314003. The red hatched area shows the region spanned by the [NII]/Hα ratio in the off-nucleus gas in TXS 2353-003. Light blue dots indicate the distribution of line ratios for galaxies in the local Universe (from SDSS; see Kauffmann et al. 2003), and the dashed blue line shows the diagnostic of Kewley et al. (2006) to separate HII regions and star-forming galaxies (below) from AGN (above). The solid blue lines indicate how the distribution of line ratios for both SF galaxies and AGN are expected to evolve out to high redshift (Kewley et al. 2013, their model 4 with metal-poor narrow-line regions): the two HzRGs are clearly consistent with the predictions for high redshift AGN.

surrounded by extended, low-surface-brightness halos. This is remarkable, given that the general population of passively evolving early-type galaxies at high redshift tends to be more compact than their local analogs (e.g., Daddi et al. 2005; van Dokkum et al. 2008; Schawinski et al. 2011; Whitaker et al. 2012). Furthermore, although about 1/3 of HzRGs are still actively star-forming (Drouart et al. 2014), their molecular gas reservoirs of a few 10^{10} $M_\odot$ (e.g., Emonts et al. 2014) compared to few 10^{11} $M_\odot$ of stellar mass (Seymour et al. 2007; De Breuck et al. 2010) suggest that most of their stellar mass growth has already been completed. Targett et al. (2011) found extended broadband emission when stacking 13 HzRGs at redshifts between $z = 1.5$ and 2.0 (as did Best et al. 1998, at slightly lower redshifts). However, only Hatch et al. (2009) have so far reported a qualitatively similar surface-brightness profile in an individual radio galaxy, MRC 1138−262 at $z = 2.16$. Previous studies, e.g., Pentericci et al. (2001), have drawn attention to the irregularity of broadband morphologies in many cases, which they attributed to the presence of on-going mergers.

4.3. Surface brightness profiles

Both galaxies are spatially resolved into four or five resolution elements in the ISAAC images, which enables us to do a basic analysis of their surface-brightness profiles shown in Fig. 6. The goal of this analysis is to demonstrate that the extended low-surface brightness regions seen in the broadband images are not just the faint extensions of the surface-brightness profiles of the central regions, but separate components of the light profiles. We are mainly interested in whether (and over what radii) the profiles are consistent with the $r^{1/4}$ or de Vaucouleurs profile typical of early-type galaxies, corresponding to a Sérsic profile with index $n = 4$ (Sérsic 1963, 1968).

The profiles shown in Fig. 6 were obtained with the IRAF task `Ellipse` (Freudling 1993), measuring the surface

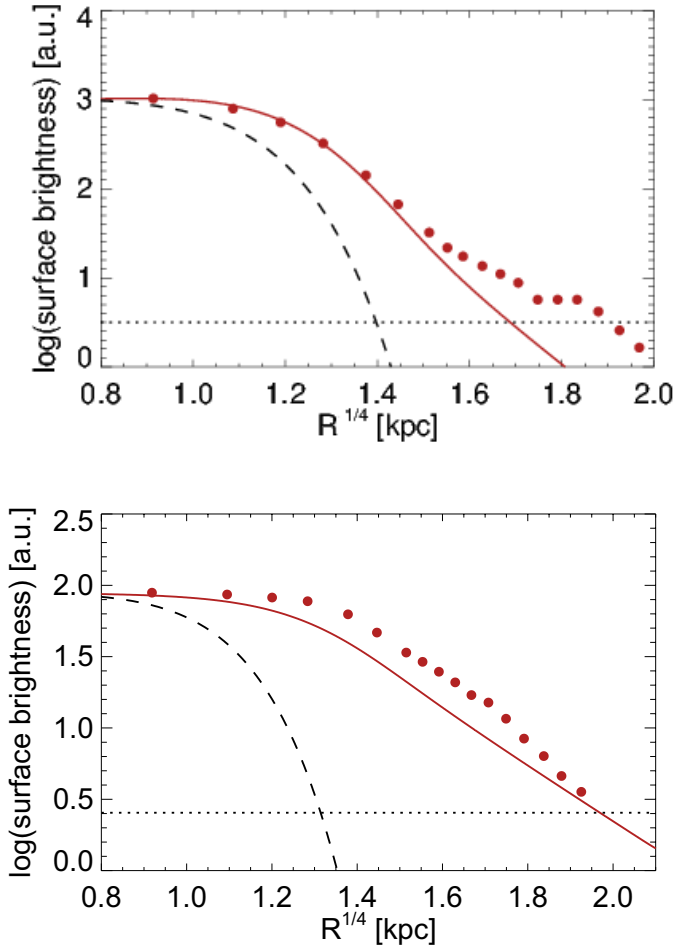

Fig. 6. Surface-brightness profiles of NVSS J210626-314003 (*top*) and TXS 2353−003 (*bottom*) extracted from ISAAC H-band and Ks-band images, respectively. Red dots show the measured azimuthally averaged surface brightnesses as a function of $R^{1/4}$. Red lines show a Sérsic fit with $n = 4$, corresponding to the de Vaucouleurs law for classical elliptical galaxies, and convolved with the point spread function in each image. The dashed black lines show the size of the seeing disk. Dotted horizonal lines show the 3σ limiting surface brightness of our images. Excess flux at large radii compared to the $R^{1/4}$ law is characteristic for brightest cluster galaxies in evolved galaxy clusters (e.g., Schombert 1987).

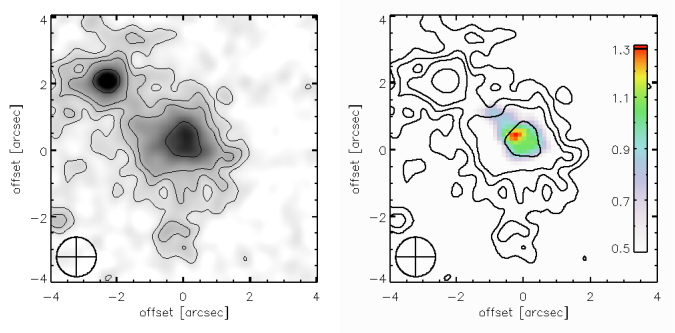

Fig. 7. *Left*: ISAAC H-band broadband image of TXS 2353−003 convolved with a two-dimensional Gaussian to match the spatial resolution of the Hα + [NII] map shown in the *right panel*. *Right*: Hα morphology of TXS 2353−003, convolved with a two-dimensional Gaussian to emphasize the morphology of the faint northeastern extension at a spatial resolution of 1.2″. The color bar shows the contamination to the flux density measured in the broadband filter from Hα line emission in units of 10^{-19} erg s^{-1} cm^{-2} Å^{-1} arcsec^{-1}. Contours show the broadband K-band morphology and are identical to those shown in the *left panel*. Starting from the outermost contour, the broadband fluxes represented by each contour are 1.1, 1.8, 2.5, and 5.4 × 10^{-19} erg s^{-1} cm^{-2} Å^{-1} arcsec^{-1} (3, 5, 7, and 15σ in the convolved image, where $\sigma = 3.9 \times 10^{-20}$ erg s^{-1} cm^{-2} Å^{-1} arcsec^{-1}). The circles in the lower left of each panel show the size of the convolved PSF.

brightness in circumnuclear elliptical annuli with radii increasing in steps of 0.1″. `Ellipse` fits the ellipticity of these annuli, finding between 0.05 and 0.4 in our case. Solid red lines in Fig. 6 show the expected curves of $n = 4$ Sérsic profiles that match the central 1″ of the light profile, with effective radii $R = 261$ kpc and $R = 15$ kpc for TXS 2353-003 and NVSS J21062-314003, respectively. These effective radii are consistent with those we found with two-dimensional fits using `Galfit` (Peng et al. 2002, 2010), which we ran on images that were slightly smoothed to minimize pixel-to-pixel noise (by convolution with a 3 × 3 pixel Gaussian) and where we left all parameters free, except imposing that $n = 4$.

The comparison between the expected profiles for $n = 4$ and the observations shown in Fig. 6 illustrates that only the inner regions of NVSS J210626−314003 can be fitted with a de Vaucouleurs profile, with radius $R_e = 15$ kpc. However, the extended halo produces residuals greater than 3σ. For TXS 2353−003, the surface-brightness contrast between the central regions and the extended outer halo is lower, resulting in a very large size of $R_e = 261$ kpc for a de Vaucouleurs profile, which matches the central and outermost isophotes, but also leads to significant residuals at intermediate radii. This is in agreement with the visual impression that only NVSS J210626−314003 has a distinctive, high-surface brightness core, whereas TXS 2353−003 is more diffuse. High-resolution imaging with the *Hubble* Space Telescope (HST), for example, would be needed for a full analysis of the surface-brightness profiles in the inner regions of our galaxies. Nonetheless, these results already show that both galaxies show important departures from simple de Vaucouleurs profiles at intermediate and large radii. Such extended wings are characteristic of central cluster galaxies (e.g., Schombert 1987).

4.4. Line contamination

Line emission in high-z radio galaxies can reach high equivalent widths and might therefore be a significant contaminant in morphology measurements through broadband filters (Pentericci et al. 2001; Nesvadba et al. 2008; Targett et al. 2011). We will now investigate the significance of this contamination in our analysis.

From our SINFONI imaging spectroscopy we know the line fluxes of the most prominent optical emission lines in both galaxies, Hα, [NII]$\lambda\lambda$6548, 6583, and [OIII]$\lambda\lambda$4959, 5007. In TXS 2353-003, the combined flux of all emission lines in the H band reaches an average surface brightness of 1.6×10^{-15} erg s^{-1} cm^{-2} arcsec^{-2} in a 2.15″ aperture around the center of the galaxy, and 3×10^{-16} erg s^{-1} cm^{-2} arcsec^{-2} along the northeastern extension. Outside this region, line emission is not detected and must therefore be below the 3σ upper surface-brightness limit of 1×10^{-16} erg s^{-1} cm^{-2} arcsec^{-2}.

The broadband morphology of TXS 2353−003 is shown in the left panel of Fig. 7 as a gray scale image and contours. The image was convolved with a two-dimensional Gaussian to a resolution of 1.2″, to match the size of the seeing disk of the Hα and [NII]λ6583 line image shown in the right panel of Fig. 7,

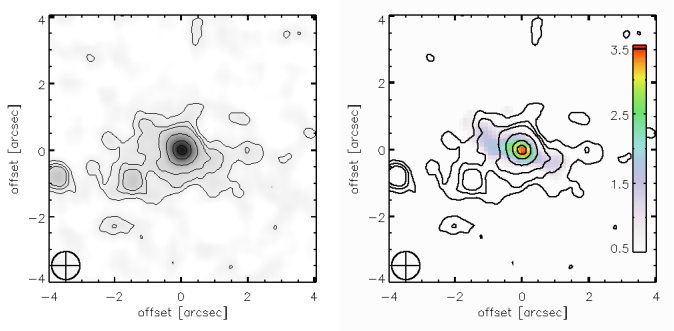

Fig. 8. *Left*: ISAAC K-band broadband image of NVSS J210626-314003 smoothed to the same spatial resolution as the SINFONI imaging spectroscopy, 1″. *Right*: Hα morphology of NVSS J210626-314003. The color bar shows the contamination to the flux density measured in the broadband filter from Hα line emission in units of 10^{-19} erg s^{-1} cm^{-2} Å^{-1} arcsec^{-1}. Contours show the broadband K-band morphology and are the same as in the *left panel*. The contour levels correspond to 3, 5, 7, 15, and 30× the root-mean square of the broadband image smoothed to the SINFONI resolution of 1″, which has rms = 3×10^{-20} erg s^{-1} cm^{-2} Å^{-1} arcsec^{-1}. The circles in the lower left of each panel show the size of the seeing disk.

and to enhance the contrast of the faint extended emission in the broadband image against the background noise.

The right panel of Fig. 7 shows the Hα+[NII] line image of TXS 2353−003, obtained by collapsing the data cube along the spectral direction over wavelengths where Hα+[NII] is detected. This makes the line morphology measurement more robust than the maps obtained from Gaussian fits to each individual pixel, in particular in the faint outer parts of the emission-line regions, and allows the measurement of the upper limits from the same image that is also used to estimate the emission-line surface brightness. Dividing by the 2700 Å width of the H-band filter of ISAAC[1], we find that line emission contributes on average 2.75×10^{-19} erg s^{-1} cm^{-2} arcsec^{-2} Å^{-1} to the measured flux density in the H band near the center of TXS 2353−003, and of 1.1×10^{-19} erg s^{-1} cm^{-2} arcsec^{-2} Å^{-1} in the northeastern periphery. Outside this extended emission-line region, the flux densities from emission lines drop to below 3.7×10^{-20} erg s^{-1} cm^{-2} arcsec^{-2} Å^{-1} (our 3σ limit). H-band surface brightnesses at the location of the extended Hα emission-line region are above 2.5×10^{-19} erg s^{-1} cm^{-2} Å^{-1} arcsec^{-2}, which suggests that line contamination does not dominate the overall broadband morphology of TXS 2353−003.

The broadband image of NVSS J210626−314004 is shown in Fig. 8 as a gray scale image with contours (left panel), and as contours on top of the Hα and [NII] line image (right panel), which was constructed in the same way as described above for TXS 2353−003. The line emission is closely approximated by Gaussian line profiles, and we therefore use the emission-line map derived from those fits and shown in Fig. 2. In a 2.15″ aperture around the nucleus, we find an average surface brightness of Hα and [NII] of 6.9×10^{-16} erg s^{-1} cm^{-2} arsec^{-2} and 2.2×10^{-16} erg s^{-1} cm^{-2} arcsec^{-2} in the periphery, respectively. This corresponds to a surface flux density of 2.3×10^{-19} and 9.4×10^{-20} erg s^{-1} cm^{-2} Å^{-1} arcsec^{-2}, respectively, after dividing by the filter width of the ISAAC K-band filter, 3000 Å[1]. Outside the ridge of extended line emission, the K-band flux densities from the lines drop to below 3×10^{-20} erg s^{-1} cm^{-2} Å^{-1} arcsec^{-2} (our 3σ limit on the emission-line surface brightness).

Line emission in NVSS J210626−314003 extends over regions of broadband isophotes of 1.5×10^{-19} erg s^{-1} cm^{-2} and brighter (Fig. 8). This comparison suggests that, outside the brightest areas seen in the Hα line image near the galaxy center, line emission is not a major contaminant of the broadband morphology in NVSS J210626−314003.

The diffuse Lyα halos discovered by Villar-Martín et al. (2002, 2003) would also produce fainter emission-line surface brightnesses than we observe here. For a typical $S\,B_{\mathrm{Ly}\alpha} = 2{-}3 \times 10^{-17}$ erg s^{-1} cm^{-2} arcsec^{-2}, we would expect Hα surface brightnesses between $2{-}5 \times 10^{-18}$ erg s^{-1} cm^{-2} arcsec^{-2}, assuming typical Lyα/Hα ratios of 8−13 (Villar-Martín et al. 2003). Dividing by the 2700 Å filter width of the ISAAC H-band filter, this would correspond to $0.7{-}1.5 \times 10^{-21}$ erg s^{-1} cm^{-2} Å^{-1} arcsec^{-2}, much lower than the surface brightness seen in the broadband filter.

5. Hα candidates surrounding TXS 2353-003

Narrowband imaging is a standard way of identifying emission-line galaxies at high redshifts, and has been successfully used to identify over-densities of actively star-forming galaxies around high-redshift galaxies for almost two decades (e.g., Chambers et al. 1996; Le Fevre et al. 1996; Kurk et al. 2004a; Venemans et al. 2007; Hatch et al. 2011; Koyama et al. 2013; Hayashi et al. 2012; Cooke et al. 2014). Most of these observations were carried out for HzRGs at $z \gtrsim 2$, where Hα falls in the K band, which is relatively free from telluric night-sky lines.

We also obtained Hα narrow-band imaging of TXS 2353-003, where Hα falls fortuitously into the NB 1.64 filter (although not perfectly into the center). Our main goal was to search for possible bright emission-line gas outside the small SINFONI field of view of 8″ × 8″, that would be associated with the environment rather than the radio galaxy itself. This also enables us to identify emission-line galaxies that are within the same dark-matter environment, and within a velocity range of −1580 km s^{-1} to +3000 km s^{-1} from the HzRG. Typical galaxy overdensities around HzRGs have velocity dispersions of <900 km s^{-1} (Venemans et al. 2007), which suggests that the asymmetry of the velocity range in our case does not hinder our detection of a potential overdensity of line emitters around the radio galaxy out to several times the velocity dispersion of the cluster. We present the results of both parts of this narrow-line imaging project in this section.

5.1. Identification of candidate Hα emitters

We identified candidate emission-line galaxies associated with the dark-matter environment of TXS 2353-003 (candidate HAEs) in two different ways. The first is a method introduced by Bunker et al. (1995) that searches for a flux excess in the narrow compared to the broadband image, and the second is the direct inspection of the continuum-subtracted line image described in Sect. 2.3.

For the flux excess method of Bunker et al. (1995), we used SExtractor v.2.5.0 (Bertin & Arnouts 1996) to construct catalogs from the narrow- and broadband images, setting the parameters `DETECT_THRESH` = 2.0 and `ANALYSIS_THRESH` = 2.0, while leaving all others at their default values. We then take the positions of the galaxies in the catalog extracted from the broadband image to perform aperture photometry within 2″ apertures in both images. Using fixed apertures is appropriate for marginally

[1] http://www.eso.org/sci/facilities/paranal/decommissioned/isaac/inst/isaac_img.html

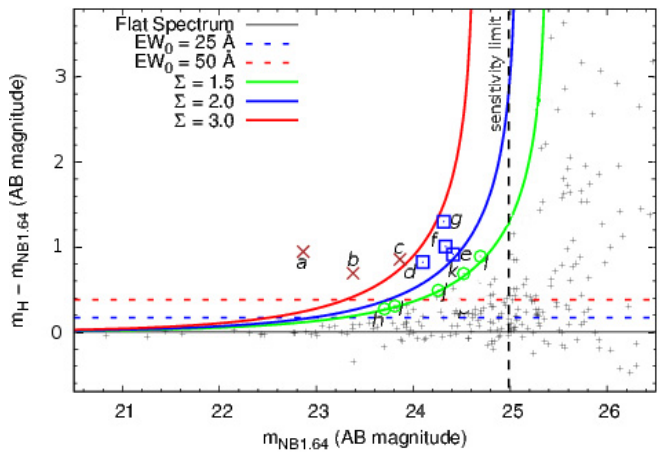

Fig. 9. Broad- to narrowband color−magnitude diagram of our candidate Hα emitters. Hα candidates are labeled with colored symbols, depending on the significance of their detection. Letters refer to the sources shown in Fig. A.1. Source "a" is the HzRG.

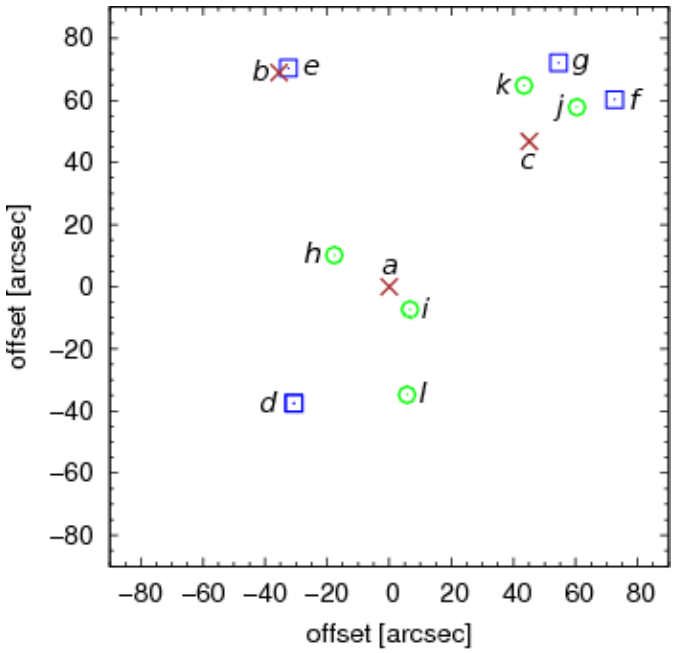

Fig. 10. Positions of the candidate Hα emitters surrounding TXS 2353-003 on the sky. The HzRG is at the field center and labeled with the symbol "a". Offsets are given relative to the position of TXS 2353-003. North is up and east to the left.

or unresolved galaxies like ours, and has the advantage of providing errors that are independent of galaxy size (see also Kurk et al. 2004a). Selecting our candidates from the broadband image, rather than the narrowband, is different from many other narrowband searches, but makes our selection particularly robust, since it requires independent detections in two images. The disadvantage is that we might miss galaxies with particularly high emission-line equivalent widths. However, comparison of the catalogs extracted from the two images shows that this was not the case in our analysis.

We use the "significance of excess", Σ, as defined by Bunker et al. (1995), i.e., "the number of standard deviations between the counts measured in the broadband and the number expected on the basis of the narrowband counts (assuming a flat spectrum)", to select the best Hα candidates. In addition, and again following Bunker et al. (1995) we require that the sources fall above a given equivalent width threshold. Following Kurk et al. (2004a), we choose $EW_0 \geq 50$ Å and 25 Å. These thresholds correspond to broad- and narrowband colors of 0.38 and 0.17, respectively. Three sources with $\Sigma \geq 3.0$ even have $EW_0 \geq 100$ Å, including the radio galaxy, which corresponds to a broad- to narrowband color of 0.69.

The resulting color−magnitude diagram is shown in Fig. 9. We find seven sources with $\Sigma \geq 2.0$ and $EW_0 \gtrsim 50$Å. We also show another seven Hα candidates that have somewhat lower excess significances $\Sigma = 1.5-2.0$. A fraction of these are probably part of the overdensity of TXS 2353-003. However, the fraction of misidentifications due to larger spectral slopes, for example, is likely to be larger among these sources, which is why we restrict our analysis to the most robust candidates above $\Sigma = 2.0$.

5.2. An overdensity of Hα candidates around TXS 2353−003

Given the good seeing of our narrowband data of 0.4″, most Hα candidates are spatially resolved (Fig. A.1) and we estimate Hα equivalent widths of 50−250 Å in the rest frame, corresponding to Hα fluxes between about 1 and a few $\times 10^{-16}$ erg s^{-1} cm^{-2}. Their properties are listed in Table 2. We did not correct the Hα flux and equivalent widths for [NII] emission, which should fall into the same filter. Observations of UV/optically selected galaxies at high redshift typically show very low [NII]/Hα line ratios on the order of 10% (e.g., Förster Schreiber et al. 2009; Lehnert et al. 2009; Queyrel et al. 2012). Using the conversion of Kennicutt (1998) with a 1−100 $M_\odot$ Salpeter initial mass function, we find star formation rates of 16−35 $M_\odot$ yr^{-1} per galaxy, and a moderate total star formation rate of 138 $M_\odot$ yr^{-1} in these galaxies combined. These values were not corrected for extinction, so intrinsic star formation rates could be higher. For example, Garn et al. (2010) and Stott et al. (2013) typically find 1 mag extinction in H-alpha meaning that intrinsic star formation rates are probably a factor of ∼2.5 times higher. The expected fraction of low-redshift interlopers is much lower in our case than for narrowband searches using Lyα. The brightest emission lines longward of Hα are the Paschen and Brackett hydrogen lines in the near-infrared, with typically much lower equivalent widths than Hα.

To quantify whether the observed number of Hα candidates around TXS 2353-003 may herald an overdensity of galaxies, we have to compare our data with samples of Hα emitters in the field at the same epoch. A blind redshift search for HAEs at $z = 1.48$ has recently been performed by Sobral et al. (2013) through the NB 1.617 filter at UKIRT, which has a very similar width of 210 Å (compared to 250 Å for our ISAAC filter), that we use as reference for the expected source density in the field. The HiZEL survey (Sobral et al. 2009, 2010, 2012, 2013) gives an estimate of the Hα emitters that we can expect in a blank field: Sobral et al. (2012) concentrated on Hα emitters at $z \simeq 1.47$, very close to the $z = 1.49$ of TXS 2353−003. They found 295 NB emitters over the 0.67 deg^2 field of their main analysis, and 411 over the entire 0.79 deg^2 field of their NB observations. Among them, 190 objects also show an excess in deep NB imaging centered on the [OII]λ3727 emission line and have colors compatible with a photometric redshift $z \simeq 1.47$. This leads to densities of candidate HAEs in the field of $\Sigma_{\rm HAE} \simeq 0.14$ HAE arcmin^{-2} (with all NB emitters); $\Sigma_{\rm HAE} \simeq 0.12$ HAE arcmin^{-2} (with NB emitters in their main field) and $\Sigma_{\rm HAE} \simeq 0.08$ HAE arcmin^{-2} (with NB emitters having an adequate photometric redshift). These values

Table 2. Parameters of the putative Hα emitters around TXS 2353-003 found in our observations.

ID	RA (J2000)	Dec (J2000)	Distance [arcmin]	NB flux[a] [0.1μJy]	BB flux[a] [μJy]	BB-NB color	EW_0[b] [Å]	Hα flux[c] [10^{-17} erg s^{-1} cm^{-2}]	SFR[d] [$M_\odot$ yr^{-1}]
a	23:55:35.58	−00:02:46.2	0.0	25.9	14.3	0.69	152.4	63.6	N/A
b	23:55:37.95	−00:01:36.8	1.29	16.2	11.3	0.95	100.2	32.1	35
c	23:55:32.56	−00:01:59.2	1.08	10.3	6.2	0.86	132.3	23.8	26
d	23:55:37.64	−00:03:23.9	0.81	8.3	5.4	0.76	112.7	18.7	20
e	23:55:37.74	−00:01:35.3	1.29	6.2	3.5	0.91	145.1	20.1	22
f	23:55:31.92	−00:01:33.8	1.51	6.7	3.5	1.01	166.8	17.1	19
g	23:55:30.72	−00:01:45.7	1.57	6.8	2.7	1.3	248.2	15.0	16

Notes. [(a)] Measured in 2″ diameter apertures. [(b)] Rest-frame equivalent width. [(c)] Assuming that the color excess in the NB image is entirely from line emission. [(d)] Following Kennicutt (1998). We do not give a star formation rate (SFR) for the radio galaxy, because the line ratios are not consistent with photoionization from young stars.

include galaxies down to a 3σ flux level of 7×10^{-17} erg s^{-1} cm^{-2}, compared to 1×10^{-17} erg s^{-1} cm^{-2} in our case.

Around TXS 2353−003, with an effective field of view of 5.4 arcmin^2 (neglecting the trimmed edges where our data did not reach the full depth) we find six Hα emitting candidates with fluxes $>7 \times 10^{-17}$ erg s^{-1} cm^{-2} and significances $\Sigma \geq 2.0$ in addition to the radio galaxy. This corresponds to a source density of 1.1 arcmin^{-2}, and an overdensity by a factor ∼8 relative to the field.

Kurk et al. (2004b) detected 28 HAEs in two ISAAC pointings around MRC 1138-262 at $z = 2.16$ down to an Hα flux limit of 2.5×10^{-17} erg s^{-1} cm^{-2}, which corresponds to the same luminosity limit as the current analysis. They found a source density of 2.2 arcmin^{-2}. Although our source density at $z = 1.5$ is lower than that in the $z = 2.16$ overdensity around MRC 1138-262 in absolute terms, the significance of the overdensity relative to the field at the same epoch is high, because the star formation rate density at $z = 1.5$ in the field is already strongly declining for the highest Hα luminosities (e.g., Sobral et al. 2013).

Finding high surface-brightness gas out to the periphery of our SINFONI data cube raises the question whether there is similarly bright line emission outside the small, 8″ × 8″ field of view of SINFONI (67 kpc × 67 kpc at $z = 1.49$). We do not find any such emission down to a 3σ detection limit of 6×10^{-20} erg s^{-1} cm^{-2} Å^{-1} in the continuum subtracted narrowband image. With the 250 Å width of the NB1.64 filter, and cosmological surface-brightness dimming by a factor $(1+z)^4 = 39$, we are sensitive to the equivalent of $\geq 60 \times 10^{-17}$ erg s^{-1} cm^{-2} arcsec^{-2} in nearby clusters. This is more than an order of magnitude fainter than the surface brightness observed, e.g., in parts of the filaments in the Perseus cluster (Hatch et al. 2007).

6. Comparison of TXS 2353-003 and NVSS J210620-214003 with cluster central galaxies

High-redshift radio galaxies do not often reside in solitude, but are surrounded by overdensities of line or continuum emitters, suggesting that a significant fraction of the HzRG population may be the progenitors of the central galaxies of massive galaxy clusters (e.g., Chambers et al. 1996; Le Fevre et al. 1996; Kurk et al. 2004a; Venemans et al. 2007; Galametz et al. 2012). Wylezalek et al. (2013) obtained *Spitzer* warm-mission IRAC photometry at 3.6 μm and 4.5 μm of 200 HzRGs, including our two sources. They find that, compared to the *Spitzer* UKDSS Ultra Deep Survey (Kim et al. 2011), 55% of HzRGs are surrounded by $\geq 2\sigma$ overdensities of galaxies with colors between the 3.6 μm and 4.5 μm channels that are consistent with redshifts $z \geq 1.3$. Like any method identifying galaxy overdensities, however, the IRAC color selection only samples parts of the population of putative satellite galaxies around HzRGs, and can therefore only provide lower limits to the actual density of such galaxies around a particular HzRG. It can therefore only demonstrate the presence, but not the absence of such an overdensity of galaxies around a given radio galaxy.

Wylezalek et al. (2013) show that TXS 2353-003 is surrounded by one of the highest overdensities of IRAC-selected sources, with an excess of $>5\sigma$, and consistent with the results of our narrowband search presented in Sect. 5. NVSS J210626-314003, however, does not stand out as a source with a particularly dense environment of IRAC-selected sources in the Wylezalek et al. (2013) sample, a 1.2σ excess. Unfortunately, the observing program committee of ESO only granted us narrowband imaging of TXS 2353-003, not of NVSS J210626-314003, so that we were unable to do a narrowband search around this galaxy. We note, however, that selecting a galaxy based on its bright radio emission already leads to significant biases toward galaxies in dense environments (e.g., Best 2000; Ramos Almeida et al. 2013; Hatch et al. 2014), and we argue in the following that the stellar component of NVSS J210626-314003 itself shows some of the characteristic signatures of cluster central galaxies.

6.1. K−z relationship

Kauffmann & Charlot (1998) argued that the observed K-band magnitude can be used to approximate the stellar mass of all but the most rapidly growing galaxies out to redshifts $z \geq 2$, with a scatter of about a factor of 2. This is consistent with the empirical tight $K - z$ relationship between observed K-band magnitudes of powerful radio galaxies and their redshifts (Lilly & Longair 1984; De Breuck et al. 2002; Willott et al. 2003; Bryant et al. 2009) and the small mass range of these galaxies in the *Spitzer* photometric survey of HzRGs by Seymour et al. (2007) and De Breuck et al. (2010).

In Fig. 11 we show where TXS 2353−003 and NVSS J210626−314003 fall relative to the $K - z$ relationship of Seymour et al. (2007) and De Breuck et al. (2010), and that of Lidman et al. (2012), who found a similar relationship for brightest cluster galaxies (BCGs). This figure shows the good agreement of our targets with both samples, as well as the self-consistency of both samples with each other (as expected if HzRGs are the progenitors of BCGs).

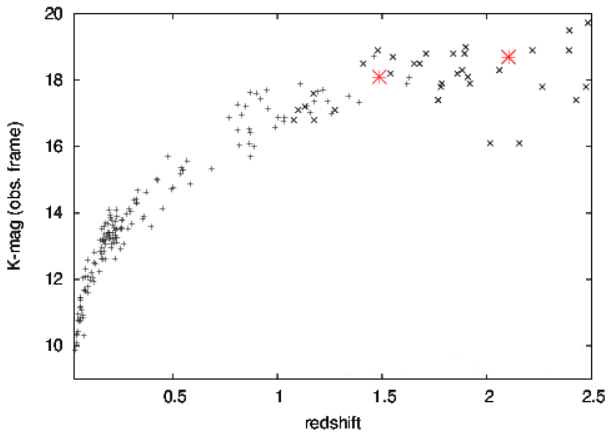

Fig. 11. Observed K-band magnitude of brightest-cluster galaxies (shown as "+") and radio galaxies (shown as "x") as a function of redshift (plot reproduced from Lidman et al. 2012). Some of the data points were taken from Stott et al. (2008, 2010). The large red stars illustrate that TXS 2353−003 and NVSS J210626−314003 fall well within the expected range of K-band magnitude, and also have typical K-band magnitudes for HzRGs at their redshifts (black crosses; Seymour et al. 2007; see also De Breuck et al. 2002; Willott et al. 2003; Bryant et al. 2009). At $z \geq 2$, Hα and [NII]$\lambda\lambda$6548,6583 fall into the K-band filter and can affect the continuum magnitudes by up to about 0.3 dex in extreme cases (Nesvadba et al. 2006).

Encouraged by the results of Kauffmann & Charlot (1998), Seymour et al. (2007), and De Breuck et al. (2010), which, when considered together, suggest that the observed K-band magnitude of HzRGs should scale with the stellar mass, we used the K-band magnitudes of $z \sim 2$ HzRGs in the Seymour et al. (2007) sample and the stellar mass estimates given in the same paper, to obtain a simple empirical relationship between stellar mass, $M_{\rm stellar}$, and observed K-band magnitude, m_K, $\log(M_{\rm stellar}/M_\odot) = 6.18-0.189\ m_K$. We find a 1σ scatter of about 0.3 dex in mass, consistent with that previously found by Kauffmann & Charlot (1998). We note that we are using observed magnitudes from galaxies in a similar redshift range, and therefore do not need a k-correction.

This allows us to derive a rough mass estimate for our two sources. For TXS 2353−003 and NVSS J210626−314003, K-band magnitudes of 18.1 ± 0.3 mag and 18.7 ± 0.2 mag suggest stellar masses in the range $\log(M^{2353}/M_\odot) = 11.1-11.4$ and $\log(M^{2106}/M_\odot) = 11.2-11.5$, respectively. While such an approach should not replace more detailed analyses of the continuum emission where additional photometric constraints are available, it does highlight that our two galaxies fall into the typical range of stellar masses of powerful radio galaxies at these redshifts.

6.2. Surface-brightness profiles

In Sect. 4.2 we showed that both galaxies are spatially resolved in our ground-based imaging, and that both have surface-brightness profiles that are not consistent with the pure Sérsic profiles of early-type galaxies ($n = 4$). The central arcsec of the profile of NVSS J210626−314003 can be fitted with a de Vaucouleurs profile with $R = 15$ kpc, but fainter extended emission persists at larger radii. TXS 2353-003 can only be fitted with a de Vaucouleurs profile when assuming an unphysically large radius of 261 kpc.

Targett et al. (2011) analyzed the K-band morphologies of 13 radio galaxies at $z = 1.5-2.5$ observed with UKIRT during very good seeing, and found that most sources are well fit with Sérsic indices $n = 3-5$ and effective radii between 5 and 10 kpc. This is in contrast to the findings of Pentericci et al. (2001) with HST/NICMOS through the *F160W* filter that only 5 out of 19 sources have well-established de Vaucouleurs profiles (although the Pentericci et al. 2001 sample does extend to higher redshifts than that of Targett et al. 2011 and, with H-band observations, samples much shorter wavelengths). Only one source of the Targett et al. (2011) sample, 0128−264, has an effective radius $R = 15$ kpc, as does NVSS J210626−314003. This galaxy is also included in our parent sample with SINFONI data. It has a small emission-line region, although elongated along the radio jet axis, and a very extended (294 kpc) radio size, resembling the two sources discussed here (Nesvadba et al., in prep.).

Massive early-type galaxies at high redshift appear to be generally characterized by their greater compactness compared to similar, more nearby galaxies (Daddi et al. 2005; van Dokkum et al. 2008, who found $R_{\rm e} \leq 1$ kpc and 0.9 kpc, respectively). Typically, these galaxies are only resolved with deep, high-resolution HST imaging, showing no deviations from Sérsic laws (e.g., Szomoru et al. 2010; Cassata et al. 2010). The HzRGs of Targett et al. (2011), which have relatively large radii (average 8 kpc) compared to submillimeter galaxies (average 3 kpc) at similar redshifts, show an average decrease in size by a factor 1.5 compared to equally massive galaxies at low redshift. A size decrease by a factor of ∼2 has also been found by Pentericci et al. (2001) for their HzRGs that are well modeled with a de Vaucouleurs profile.

Extended stellar envelopes are a primary characteristic of central cluster galaxies in the low-redshift Universe (cD galaxies; e.g., Schombert 1987), and likely formed from the debris of repeated accretion of several satellite galaxies. This interpretation also agrees with the finding of Targett et al. (2011) that HzRGs fall onto the same Kormendy relationship between central surface brightness and effective radius as massive low-redshift galaxies, which, as stated by the authors, would imply that the size increase from $z \sim 2$ to today must be accommodated by an increase in stellar mass at large galactocentric radii, as could be produced by repeated accretion of satellites. Best et al. (1998) identified similar structures in a stack of 12 radio galaxies from the 3CRR sample at $z = 0.6-1.4$, but to our knowledge, the only example of a HzRG with extended stellar halo at greater redshift currently known in the literature is MRC 1138−262 at $z = 2.2$ (the Spiderweb Galaxy, Miley et al. 2006). Hatch et al. (2008, 2009) discussed the envelope around this source in detail, finding that the rest-frame UV colors of the faint continuum emission are consistent with a stellar envelope (rather than scattering from a dusty gaseous halo) with a formation history that is coeval with that of the high-surface brightness central regions. This is in contrast to semi-analytical simulations which postulate that such envelopes assembled gradually through dry mergers over cosmological timescales (e.g., De Lucia & Blaizot 2007).

7. The nature of the extended ionized gas

A good alignment between jet and gas is typical of distant radio galaxies (the alignment effect; e.g., Cimatti et al. 1993), and this alignment was also among the prime arguments of Collet et al. (in prep.) and of Nesvadba et al. (2006, 2008) that jet and gas are physically related in their SINFONI samples of HzRG. They also found very large, super-gravitational velocity gradients reaching to more than 1000 km s^{-1} associated with the

most powerful radio sources, and broad line widths in the extended gas with $FWHM \gtrsim 800$ km s^{-1}. They considered this as evidence of fast, AGN-driven outflows in HzRGs.

None of this applies here. Velocity gradients are well below 1000 km s^{-1}, line widths outside of the central regions are only on the order of 200−300 km s^{-1}, and the mismatch in position angle between jet and gas is striking. This mismatch makes it difficult to postulate that jet cocoons are driving the gas out as they expand through the ambient gas, because it appears unavoidable in this model that cocoon (and hence, jet) and gas are cospatial, both in three dimensions and in projection.

The presence of this off-axis component of line emission is worth discussing, as is the absence of bright, extended emission-line regions along the jet axis. TXS 2353−003 may have a faint, not well resolved emission-line component along the jet axis and within the galaxy itself. However, this does not stand out compared to the gas in other regions of the galaxy, and is therefore difficult to associate uniquely with the radio jet. We find no similar emission at larger radii, including the cluster scales that we cover with ISAAC around TXS 2353-003 (Sect. 5).

The absence of bright gas on scales much larger than the host galaxy cannot be a mere observational effect, since the sensitivities of these data are comparable to the overall sample, and the surface brightness of the line emission in our targets is not significantly lower than in other HzRGs with SINFONI data. However, for the largest sources with "regular" line emission, in particular MRC 2104-242 at $z = 2.5$, the extended line emission can become very faint and is concentrated along long, thin, very filamentary structures, suggesting that the warm gas is either being heated to temperatures $T \gg 10^4$ K, or becoming strongly dispersed as the cocoon continues to expand (Nesvadba et al., in prep.; see also Pentericci et al. 2001 who observed the same gas as faint, extended filaments in their HST/NICMOS broadband imaging).

We stress that finding extended gas around HzRGs that is unrelated to the radio jets is by itself not uncommon. Many HzRGs are surrounded by diffuse halos of warm ionized gas (Villar-Martín et al. 2003), however, dense, high-surface-brightness Lyα emission consistent with the Hα surface brightnesses that we observe here is only found within the jet cocoon in the galaxies of Villar-Martín et al. (2003) Hα associated with the diffuse ionized gas would be about 2 orders of magnitude fainter than what we observe.

We will now discuss several hypotheses, from AGN orientation to galaxy interactions to extended gas disks or filaments within the radio galaxy itself or its immediate surroundings, to explain the nature of this gas.

7.1. Partial AGN illumination of ambient halo clouds

The line ratios of both sources suggest that they are photoionized by the central AGN (Sect. 3). This could imply that they do not represent a distinct structure, but are merely part of a population of ambient clouds that are distributed over large solid angles, and of which a subset is being lit up as it intercepts the quasar ionization cone. Filaments of neutral gas have also been observed around some HzRGs (van Ojik et al. 1997; Jarvis et al. 2003; Wilman et al. 2004; De Breuck et al. 2005; Nesvadba et al. 2009; Emonts et al. 2014).

However, not all HzRGs show signatures of neutral gas clouds in their halos. van Ojik et al. (1997) found Lyα absorption only in galaxies with radio sizes <50 kpc, in stark contrast to the large radio sizes, ≳200 kpc, of TXS 2353-003 and NVSS 210626-314003. Binette et al. (2000) showed from an analysis of the ionization properties that these absobers must also lie at larger radii than the radio source. In the more compact radio galaxies, Lyα absorbers are found not only against the nucleus, but also against more extended Lyα emission around the galaxy (Kurk et al. 2004a), which suggests that this result holds for large solid angles around the radio galaxies, and not just along the radio jet axis.

This scenario would also require a misalignment between radio jet axis and quasar illumination cone, as is possible because of jet precession, or a misalignment between jet axis and the normal of the torus, for example. Drouart et al. (2014) recently argued, based on *Spitzer* mid-infrared imaging and the core-to-lobe fraction of the radio sources, that the unified model must hold for the global population of HzRGs, but the presence of nuclear broad Hα emission in a few sources does also suggest that this might not be the case for each individual HzRG (Nesvadba et al. 2011a).

Alternatively, we may be seeing gas in an old cocoon from a previous radio-loud activity phase of the super-massive black hole. Jet precession has been invoked to explain the X-shaped radio sources at low redshift, where about 5−10% of FRII radio sources have two pairs of radio lobes (Leahy & Muxlow 2002). The second bar of the "X", typically secondary pairs of fairly diffuse, low surface-brightness wings in centimeter radio continuum imaging, may be the relic of a previous burst of nuclear activity along a different jet axis. Detecting such low surface-brightness emission directly would be very challenging at high redshift.

This scenario, however, also has its difficulties. Kaiser & Cotter (2002) argued that clouds in relic cocoons will be destroyed by shocks within a few 10^6 yrs, which is of the same order as the ages of bright radio sources in high-redshift galaxies (e.g., Blundell & Rawlings 1999). In the cocoon model, dense clouds are confined by the high pressure of the cocoon material, and should disperse within a sound-crossing time once the jet has stopped maintaining the cocoon pressure high (e.g., Fabian et al. 1987). From the size of the two lobes in our sources, 310 kpc and 190 kpc, and assuming a jet advance speed on the order of $0.1c$, we can roughly constrain that the feeding of a putative older jet component must have ended at least about 1×10^7 yrs ago in our two sources, so that most of the emission-line clouds should have already been destroyed or evaporated. The relatively old age of our two sources does not make them good candidates for seeing relic cocoons, in particular since many younger radio sources, which should in principle have brighter relic cocoons, do not show evidence of two sets of radio lobes or extended emission-line regions.

We conclude that neither partial AGN illumination of a general population of ambient clouds nor repeated cycles of radio-loud AGN activity with different jet orientations appears to be a good explanation for the nature of our sources.

7.2. External gas supply from a satellite galaxy?

Gas transfer from a satellite galaxy undergoing accretion onto the HzRG, as previously observed in the $z = 3.8$ HzRG 4C60.07 (Ivison et al. 2008), is another interesting hypothesis for the origin of this misaligned gas in our two sources. In this case, the extended line emission could trace a gas tail produced by ram-pressure stripping or tidal forces. However, only TXS 2353−003 has a companion along the direction of the extended gas, but at a larger distance from the radio galaxy. NVSS J210626-314003 has no obvious companion within several tens of kpc that can be associated with the extended emission-line region.

It is uncertain whether the galaxy near TXS 2353-003 (Fig. 1) is physically associated with the radio galaxy, although its infrared colors as measured with IRAC are consistent with a redshift $z \gtrsim 1.3$ using the criteria of Papovich (2008) (Sect. 5). However, we detect no Hα line emission down to 3.3×10^{-18} erg s^{-1} cm^{-2}. Tidal forces during galaxy interactions produce extended tails, and also funnel gas toward the nuclei of the galaxies (e.g., Barnes & Hernquist 1996), fueling intense nuclear starbursts. Likewise ram pressure should not only strip parts of the ISM, but also compress the gas along the head of the infalling galaxy, enhancing the gas surface brightness within the galaxy, and potentially star formation (Kapferer et al. 2008).

It appears therefore difficult for a galaxy to produce a tail of $\sim 10^9$ $M_\odot$ of ionized gas without sustaining significant star formation. Our upper limit of Hα flux corresponds to star formation rates on the order of 10 $M_\odot$ yr^{-1} (using the Kennicutt 1998 calibration and neglecting extinction). Since the source is bright in the continuum at similar wavelengths, the Hα equivalent width must also be low. Although gas, dust, and young stars are not necessarily co-spatial (Calzetti 1997), this would imply here that the galaxy, in spite of losing considerable fractions of its ISM in the putative tail, is also maintaining a highly efficient obscuring dust screen around its star-forming regions. This appears contradictory, in particular for high-z galaxies, which typically have extended star formation in multiple knots across the galaxy (e.g., Förster Schreiber et al. 2009). Other HzRGs, e.g., MRC 1138-262 at $z = 2.16$, are already known to be surrounded by companions within a few tens of kpc that are already on the red sequence (Kodama et al. 2007) and lack line emission (Nesvadba et al. 2006; Kuiper et al. 2011). It thus appears unlikely that external gas supply from a satellite galaxy is a good explanation of the extended emission-line regions in our galaxies.

7.3. Extended gas disks within the radio galaxy

Best (2000) pointed out that radio galaxies with very extended radio sources are particularly good candidates for being cluster central galaxies because the pressure from the Mpc-scale intracluster medium boosts the luminosity of the radio source even for comparably extended jets (see also Athreya et al. 1998; Klamer et al. 2006). Many authors have previously suggested that the progenitors of brightest cluster galaxies are likely to be found among HzRGs (e.g., Pentericci et al. 2001; Miley et al. 2006; Hatch et al. 2009), and Wylezalek et al. (2013) find from IRAC imaging that TXS 2353-003 is even associated with the most strongly pronounced overdensity within their sample.

The gas that we see here may actually have much in common with the extended gas disks or filaments that are found in and near cluster central galaxies in the more nearby Universe. Mismatches between the position angles of jet and gas are fairly common in about 30% (McDonald et al. 2010) of cool-core galaxy clusters with extended Hα filaments. A particularly clear example, where the warm ionized gas appears to avoid the cavities that the radio jet has inflated in the intracluster medium is Abell 1795, in particular at the highest emission-line surface brightnesses (van Breugel et al. 1984). In total, such structures have up to a few 10^{10} $M_\odot$ (e.g., Salomé et al. 2006) of warm and cold gas with $T \leq 10^4$ K, typically dominated by cold molecular gas. We have already argued in Sect. 6 that our sources follow the overall trends found in BCGs between Hα luminosity and surface luminosity, size, and ratios of low-ionization emission lines.

Imaging spectroscopy of cool-core clusters with bright optical line emission (e.g., Hatch et al. 2006, 2007; Wilman et al. 2006, 2009; Farage et al. 2010, 2012) shows that the gas has typically $FWHM \sim 100$–300 km s^{-1} outside the near-nuclear regions, with a characteristic broadening toward the center, with typical $FWHM \geq 500$ km s^{-1} and up to the values we find near the center of NVSS J210626−314003 and TXS 2353−003 (Sect. 3 and Figs. 1 and 2). However, regular velocity gradients of a few 100 km s^{-1}, similar to what we observe in our sources, are found only in some BCGs, e.g., Abell 262 (Hatch et al. 2007) or 2A 0335+096 (Farage et al. 2012). Alternatively, disks with well-ordered velocity fields, perhaps more like in NVSS J210626-3140003 than in TXS 2353−003, have also been found, for example in Hydra A (Hamer et al. 2014). Such disks are also typically not aligned with the radio jet axis, but can be illuminated by the central AGN, in particular if the opening angle of the AGN illumination cone is large.

The observed velocity gradients in our two sources are in fact consistent with rotational motion in a gravitational potential as suggested by the stellar mass estimates of 1.5–3×10^{11} $M_\odot$ (Sect. 6.1). A dynamical mass estimate, v, can be derived by setting $v = \sqrt{M \sin i^2 G/R}$, where M is the stellar mass, R the radius of the putative disk, i the inclination angle, and G the gravitational constant. With $R = 10.5$ kpc, measured for the very regular velocity field of NVSS J210626-314003, we find $v = 250$–$350 \sin i^{-1}$ km s^{-1}, compared to 220 km s^{-1} observed. Even if the gradients were dominated by radial outflow motion, the small velocity range implies that most of this gas is unlikely to escape.

This is consistent with the finding that the gas extends over similar radii to the faint continuum wings in the ISAAC image of TXS 2353-003 on both sides, and in NVSS J210626-314003 on the southwestern side. If the wings in the continuum surface brightness profiles of our two sources represent extended stellar halos (Hatch et al. 2009), perhaps originating from a phase of rapid accretion of many satellite galaxies in the very early evolution of the HzRGs (Burkert et al. 2008), then we may be seeing leftover gas that is settling down after this phase. McDonald et al. (2010) suggested that the condensation of such gas into fairly dense clouds could be accelerated by weak shocks caused by the passage of a companion galaxy, as may be the case for the putative companion in TXS2353-003.

Weak shocks could also be produced by the vestiges of the relic cocoon that initially formed when the jet was passing through the inner regions of the halo. This scenario has some resemblance to the cyclical AGN feedback scenarios invoked, e.g., by Pizzolato & Soker (2005) or Antonuccio-Delogu & Silk (2010) to explain extended gas disks and filaments in nearby cluster central galaxies. Nesvadba et al. (2010, 2011b) argued that isolated radio galaxies with extended gas disks may also require repeated, episodic AGN activity, broadly akin to the Pizzolato & Soker (2005) model, in order to understand the observed properties of the gas. Winds associated with the large radio jets we observe may have dispersed the ISM of these galaxies just a few 10^7 yrs ago, and parts of this gas may now be raining back onto the galaxy, possibly feeding a new feedback cycle. The age of the Universe at $z = 1.5$–2 is already >3 Gyr, so that repeated activity cycles are possible for duty cycles of a few times 10^8 yrs, as seems appropriate at low redshift (Pizzolato & Soker 2005). The gas cooling times could be lowered by compression of the outflow and diffuse ambient gas that is being swept up as the two bubbles of the AGN cocoon continue to inflate in the form of a momentum-driven wind after the feeding from the

AGN has ceased (Kaiser & Cotter 2002). This cyclical feedback may contribute to forming the hot intracluster X-ray gas in massive galaxy clusters today, which presumably took place around redshift $z \geq 2$ (Nath & Roychowdhury 2002; McCarthy et al. 2008). Energy injection through repeated episodic AGN activity has also been invoked as an explanation of how the X-ray halos surrounding individual massive early-type galaxies can be maintained over a Hubble time (e.g., Mathews & Brighenti 2003; Best et al. 2006).

8. Summary

We have presented an analysis of rest-frame optical imaging spectroscopy and deep broadband near-infrared imaging of two radio galaxies at $z \sim 2$, which have extended emission-line regions that are strongly misaligned relative to the axis of the radio jets. This is in stark contrast to the majority of powerful radio galaxies at similar redshifts, where the gas is aligned within 20−30° of the jet axis, as expected from a cocoon of turbulent gas that is being inflated by the expanding radio jets. For one source, TXS 2353-003 at $z = 1.5$, we also present Hα narrowband imaging through the [FeII]1.64 filter of ISAAC, finding an overdensity of Hα candidates which resembles those of radio galaxies at higher redshift.

The gas in both galaxies is less perturbed than in radio galaxies with more typical gas properties. In particular, line widths in the extended gas are lower and, with $FWHM \sim 200$−300 km s^{-1} comparable to those in the extended gas disks and filaments surrounding brightest cluster galaxies at lower redshifts. Overall, we find remarkable similarities to the BCGs in low-redshift cool-core clusters, ranging from the extended, faint continuum halos in both galaxies that are atypical for massive high-redshift galaxies except for the particularly well-studied Spiderweb Galaxy MRC 1138-262, where such structures are interpreted as extended stellar halos broadly akin to cD galaxies at lower redshifts. Both galaxies fall onto the relationship between K-band magnitude and redshift for brightest cluster galaxies and HzRGs, suggesting they are among the most massive galaxies at their epoch. We note that, given that HzRGs are now generally considered to be the progenitors of BCGs, the distinction between both classes is not mutually exclusive, and our two sources may simply be further evolved than many other HzRGs, but still following the same overall evolutionary path.

We discuss several scenarios for the nature of this gas, finding that simple illumination effects in otherwise typical HzRG halos is not a good explanation, and neither are galaxy interactions. Generally speaking, our results support the hypothesis that the extended line emission arises from extended gas disks or filaments within or near the radio galaxy, by analogy with broadly similar structures in nearby cluster central galaxies. This could be evidence for cyclical AGN feedback, which has been discussed on several occasions for nearby clusters.

Acknowledgements. We are very grateful to the staff at Paranal for having carried out the observations on which our analysis is based. We also thank the anonymous referee for the detailed comments which helped improve the paper. C.C. wishes to acknowledge support from the Ecole Doctorale Astronomie & Astrophysique de l'Ile de France. Parts of this research were conducted by the Australian Research Council Centre of Excellence for All-sky Astrophysics (CAASTRO), through project number CE110001020.

References

Adams, J. J., Hill, G. J., & MacQueen, P. J. 2009, ApJ, 694, 314
Antonuccio-Delogu, V., & Silk, J. 2010, MNRAS, 405, 1303
Archibald, E. N., Dunlop, J. S., Hughes, D. H., et al. 2001, MNRAS, 323, 417
Athreya, R. M., Kapahi, V. K., McCarthy, P. J., & van Breugel, W. 1998, A&A, 329, 809
Baldwin, J. A., Phillips, M. M., & Terlevich, R. 1981, PASP, 93, 5
Barnes, J. E., & Hernquist, L. 1996, ApJ, 471, 115
Barthel, P., Haas, M., Leipski, C., & Wilkes, B. 2012, ApJ, 757, L26
Baum, S. A., & McCarthy, P. J. 2000, AJ, 119, 2634
Begelman, M. C., & Cioffi, D. F. 1989, ApJ, 345, L21
Bertin, E., & Arnouts, S. 1996, A&AS, 117, 393
Best, P. N. 2000, MNRAS, 317, 720
Best, P. N., Longair, M. S., & Roettgering, H. J. A. 1998, MNRAS, 295, 549
Best, P. N., Kaiser, C. R., Heckman, T. M., & Kauffmann, G. 2006, MNRAS, 368, L67
Binette, L., Kurk, J. D., Villar-Martín, M., & Röttgering, H. J. A. 2000, A&A, 356, 23
Blundell, K. M., & Rawlings, S. 1999, Nature, 399, 330
Bryant, J. J., Johnston, H. M., Broderick, J. W., et al. 2009, MNRAS, 395, 1099
Bunker, A., Warren, S., Hewett, P., & Clements, D. 1995, MNRAS, 273, 513
Burkert, A., Naab, T., Johansson, P. H., & Jesseit, R. 2008, ApJ, 685, 897
Calzetti, D. 1997, AJ, 113, 162
Cassata, P., Giavalisco, M., Guo, Y., et al. 2010, ApJ, 714, L79
Chambers, K. C., Miley, G. K., & Joyce, R. R. 1988, ApJ, 329, L75
Chambers, K. C., Miley, G. K., van Breugel, W. J. M., et al. 1996, ApJS, 106, 247
Cimatti, A., di Serego-Alighieri, S., Fosbury, R. A. E., Salvati, M., & Taylor, D. 1993, MNRAS, 264, 421
Cooke, E. A., Hatch, N. A., Muldrew, S. I., Rigby, E. E., & Kurk, J. D. 2014, MNRAS, 440, 3262
Daddi, E., Renzini, A., Pirzkal, N., et al. 2005, ApJ, 626, 680
Davé, R., Finlator, K., & Oppenheimer, B. D. 2011, MNRAS, 416, 1354
De Breuck, C., van Breugel, W., Röttgering, H., et al. 2001, AJ, 121, 1241
De Breuck, C., van Breugel, W., Stanford, S., et al. 2002, ApJ, 123, 637
De Breuck, C., Neri, R., & Omont, A. 2003, New Astron. Rev., 47, 285
De Breuck, C., Downes, D., Neri, R., et al. 2005, A&A, 430, L1
De Breuck, C., Seymour, N., Stern, D., et al. 2010, ApJ, 725, 36
De Lucia, G., & Blaizot, J. 2007, MNRAS, 375, 2
Draper, P. W., Gray, N., Berry, D. S., & Taylor, M. 2014, Astrophysics Source Code Library [record ascl:1403.024]
Drouart, G., De Breuck, C., Vernet, J., et al. 2014, A&A, 566, A53
Emonts, B. H. C., Norris, R. P., Feain, I., et al. 2014, MNRAS, 438, 2898
Fabian, A. C., Crawford, C. S., Johnstone, R. M., & Thomas, P. A. 1987, MNRAS, 228, 963
Farage, C., McGregor, P., Dopita, M., & Bicknell, G. 2010, ApJ, 724, 267
Farage, C., McGregor, P., & Dopita, M. 2012, ApJ, 747, 28
Förster Schreiber, N. M., Genzel, R., Bouché, N., et al. 2009, ApJ, 706, 1364
Freudling, W. 1993, in ESO Conf. Workshop Proc., 47, eds. P. Grosbol & R. de Ruijsscher, 27
Galametz, A., Stern, D., De Breuck, C., et al. 2012, ApJ, 749, 169
Garn, T., Sobral, D., Best, P. N., et al. 2010, MNRAS, 402, 2017
Groves, B. A., Heckman, T. M., & Kauffmann, G. 2006, MNRAS, 371, 1559
Hamer, S. L., Edge, A. C., Swinbank, A. M., et al. 2014, MNRAS, 437, 862
Hatch, N. A., Crawford, C., Johnstone, R., & Fabian, A. 2006, MNRAS, 367, 433
Hatch, N. A., Crawford, C., & Fabian, A. 2007, MNRAS, 380, 33
Hatch, N., Overzier, R., Röttgering, H., Kurk, J., & Miley, G. 2008, MNRAS, 383, 931
Hatch, N. A., Overzier, R. A., Kurk, J. D., et al. 2009, MNRAS, 395, 114
Hatch, N. A., Kurk, J. D., Pentericci, L., et al. 2011, MNRAS, 415, 2993
Hatch, N. A., Wylezalek, D., Kurk, J. D., et al. 2014, MNRAS, 445, 280
Hayashi, M., Kodama, T., Tadaki, K.-i., Koyama, Y., & Tanaka, I. 2012, ApJ, 757, 15
Ivison, R., Morrison, G., Biggs, A., et al. 2008, MNRAS, 390, 1117
Ivison, R. J., Smail, I., Amblard, A., et al. 2012, MNRAS, 425, 1320
Jarvis, M. J., Wilman, R. J., Röttgering, H. J. A., & Binette, L. 2003, MNRAS, 338, 263
Kaiser, C. R., & Cotter, G. 2002, MNRAS, 336, 649
Kapferer, W., Kronberger, T., Ferrari, C., Riser, T., & Schindler, S. 2008, MNRAS, 389, 1405
Kauffmann, G., & Charlot, S. 1998, MNRAS, 297, L23
Kauffmann, G., Heckman, T. M., White, S. D. M., et al. 2003, MNRAS, 341, 54
Kennicutt, R. 1998, ARA&A, 36, 189
Kewley, L. J., Groves, B., Kauffmann, G., & Heckman, T. 2006, MNRAS, 372, 961
Kewley, L. J., Dopita, M. A., Leitherer, C., et al. 2013, ApJ, 774, 100
Kim, M., Dunlop, J. S., Lonsdale, C. J., et al. 2011, in BAAS 43, AAS Meet. Abstr., 217, 335.51
Klamer, I. J., Ekers, R. D., Sadler, E. M., et al. 2005, ApJ, 621, L1
Klamer, I. J., Ekers, R. D., Bryant, J. J., et al. 2006, MNRAS, 371, 852

Kodama, T., Tanaka, I., Kajisawa, M., et al. 2007, MNRAS, 377, 1717
Koyama, Y., Kodama, T., Tadaki, K.-i., et al. 2013, MNRAS, 428, 1551
Kuiper, E., Hatch, N., Miley, G., et al. 2011, MNRAS, 415, 2245
Kurk, J., Cimatti, A., di Serego Alighieri, S., et al. 2004a, A&A, 422, L13
Kurk, J., Pentericci, L., Röttgering, H., & Miley, G. 2004b, A&A, 428, 793
Leahy, J. P., & Muxlow, T. W. B. 2002, in The Universe at Low Radio Frequencies, eds. A. Pramesh Rao, G. Swarup, & Gopal-Krishna, IAU Symp., 199, 179
Le Fevre, O., Deltorn, J. M., Crampton, D., & Dickinson, M. 1996, ApJ, 471, L11
Lehnert, M. D., Nesvadba, N. P. H., Tiran, L. L., et al. 2009, ApJ, 699, 1660
Le Tiran, L., Lehnert, M., van Driel, W., Nesvadba, N., & Di Matteo, P. 2011, A&A, 534, L4
Lidman, C., Suherli, J., Muzzin, A., et al. 2012, MNRAS, 427, 550
Lilly, S. J., & Longair, M. S. 1984, MNRAS, 211, 833
Mathews, W. G., & Brighenti, F. 2003, ARA&A, 41, 191
McCarthy, I. G., Babul, A., Bower, R. G., & Balogh, M. L. 2008, MNRAS, 386, 1309
McDonald, M., Veilleux, S., Rupke, D., & Mushotzky, R. 2010, ApJ, 721, 1262
Miley, G. K., Overzier, R. A., Zirm, A. W., et al. 2006, ApJ, 650, L29
Nath, B. B., & Roychowdhury, S. 2002, MNRAS, 333, 145
Nesvadba, N., Lehnert, M., Eisenhauer, F., et al. 2006, ApJ, 650, 693
Nesvadba, N. P. H., Lehnert, M. D., De Breuck, C., Gilbert, A., & van Breugel, W. 2007, A&A, 475, 145
Nesvadba, N., Lehnert, M., De Breuck, C., Gilbert, A., & Van Breugel, W. 2008, A&A, 491, 407
Nesvadba, N. P. H., Neri, R., De Breuck, C., et al. 2009, MNRAS, 395, L16
Nesvadba, N. P. H., Boulanger, F., Salomé, P., et al. 2010, A&A, 521, A65
Nesvadba, N. P. H., De Breuck, C., Lehnert, M. D., et al. 2011a, A&A, 525, A43
Nesvadba, N. P. H., Polletta, M., Lehnert, M. D., et al. 2011b, MNRAS, 415, 2359
Ogle, P., Davies, J. E., Appleton, P. N., et al. 2012, ApJ, 751, 13
Overzier, R. A., Harris, D. E., Carilli, C. L., et al. 2005, A&A, 433, 87
Overzier, R. A., Nesvadba, N. P. H., Dijkstra, M., et al. 2013, ApJ, 771, 89
Papovich, C. 2008, ApJ, 676, 206
Peng, C., Ho, L., Impey, C., & Rix, H. 2002, AJ, 124, 266
Peng, C., Ho, L., Impey, C., & Rix, H. 2010, AJ, 139, 2097
Pentericci, L., McCarthy, P. J., Röttgering, H. J. A., et al. 2001, ApJS, 135, 63
Pizzolato, F., & Soker, N. 2005, ApJ, 632, 821
Queyrel, J., Contini, T., Kissler-Patig, M., et al. 2012, A&A, 539, A93
Ramos Almeida, C., Bessiere, P. S., Tadhunter, C. N., et al. 2013, MNRAS, 436, 997
Reuland, M., Röttgering, H., van Breugel, W., & De Breuck, C. 2004, MNRAS, 353, 377
Salomé, P., Combes, F., Edge, A., et al. 2006, A&A, 454, 437
Schawinski, K., Treister, E., Urry, C. M., et al. 2011, ApJ, 727, L31
Schombert, J. M. 1987, ApJS, 64, 643
Sérsic, J. 1963, Boletin de la Asociacion Argentina de Astronomia La Plata Argentina, 6, 41
Sérsic, J. 1968, Atlas de galaxias australes (Cordoba: Observatorio Astronomico)
Seymour, N., Stern, D., De Breuck, et al. 2007, ApJS, 171, 353
Seymour, N., Altieri, B., De Breuck, C., et al. 2012, ApJ, 755, 146
Sobral, D., Best, P., Geach, J., et al. 2009, MNRAS, 398, 75
Sobral, D., Best, P. N., Geach, J. E., et al. 2010, MNRAS, 404, 1551
Sobral, D., Best, P. N., Matsuda, Y., et al. 2012, MNRAS, 420, 1926
Sobral, D., Smail, I., Best, P. N., et al. 2013, MNRAS, 428, 1128
Solórzano-Iñarrea, C., Tadhunter, C. N., & Bland-Hawthorn, J. 2002, MNRAS, 331, 673
Stott, J. P., Edge, A. C., Smith, G. P., Swinbank, A. M., & Ebeling, H. 2008, MNRAS, 384, 1502
Stott, J. P., Collins, C. A., Sahlén, M., et al. 2010, ApJ, 718, 23
Stott, J. P., Sobral, D., Bower, R., et al. 2013, MNRAS, 436, 1130
Swinbank, A. M., Chapman, S. C., Smail, I., et al. 2006, MNRAS, 371, 465
Szomoru, D., Franx, M., van Dokkum, P. G., et al. 2010, ApJ, 714, L244
Targett, T. A., Dunlop, J. S., McLure, R. J., et al. 2011, MNRAS, 412, 295
van Breugel, W., Heckman, T., & Miley, G. 1984, ApJ, 276, 79
van Dokkum, P., Franx, M., Kriek, M., et al. 2008, ApJ, 677, L5
van Ojik, R., Röttgering, H., Miley, G., & Hunstead, R. 1997, A&A, 317, 358
Veilleux, S., & Osterbrock, D. E. 1987, ApJS, 63, 295
Venemans, B. P., Röttgering, H. J. A., Miley, G. K., et al. 2007, A&A, 461, 823
Villar-Martín, M., Vernet, J., di Serego Alighieri, S., et al. 2002, MNRAS, 336, 436
Villar-Martín, M., Vernet, J., di Serego Alighieri, S., et al. 2003, MNRAS, 346, 273
Wagner, A. Y., Bicknell, G. V., & Umemura, M. 2012, ApJ, 757, 136
Whitaker, K., Kriek, M., van Dokkum, P., et al. 2012, ApJ, 745, 179
Willott, C., Rawlings, S., Jarvis, M., & Blundell, K. 2003, MNRAS, 339, 173
Wilman, R. J., Jarvis, M. J., Röttgering, H. J. A., & Binette, L. 2004, MNRAS, 351, 1109
Wilman, R. J., Gerssen, J., Bower, R. G., et al. 2005, Nature, 436, 227
Wilman, R., Edge, A., & Swinbank, A. 2006, MNRAS, 371, 93
Wilman, R., Edge, A., & Swinbank, A. 2009, MNRAS, 395, 1355
Wylezalek, D., Galametz, A., Stern, D., et al. 2013, ApJ, 769, 79

Pages 16 to 17 are available in the electronic edition of the journal at http://www.aanda.org

Appendix A: Candidate Hα emitting galaxies around TXS 2353-003

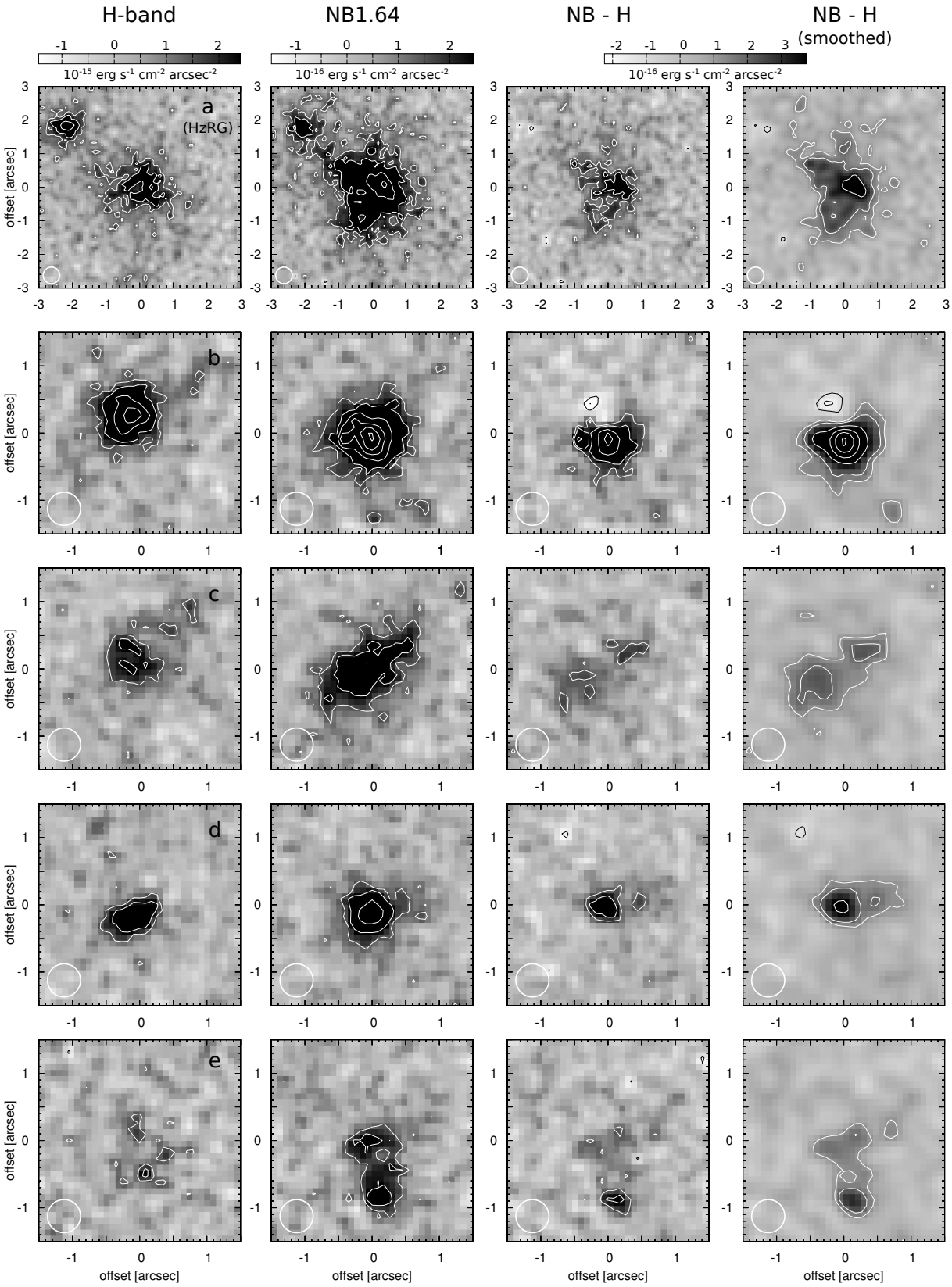

Fig. A.1. Hα emitters around TXS 2353-003 selected by the Bunker plot and confirmed when subtracting the continuum from the NB image. *Left column*: *H*-band images of the candidates. *Middle column*: NB1.64 images of the candidates. *Right columns*: continuum-subtracted NB images of the candidates, the *last column* showing them smoothed with a Gaussian kernel of $\sigma = 1$ pixel. The color palette spans -3σ to $+5\sigma$ in each case in order to highlight the faint features of these HAE candidates. The contours give the morphology of the sources at larger surface brightnesses: white contours are at levels 3; 5; 10; 15; 20 σ and the black contours are at levels -10; -5; -3σ. The HzRG is labeled "a".

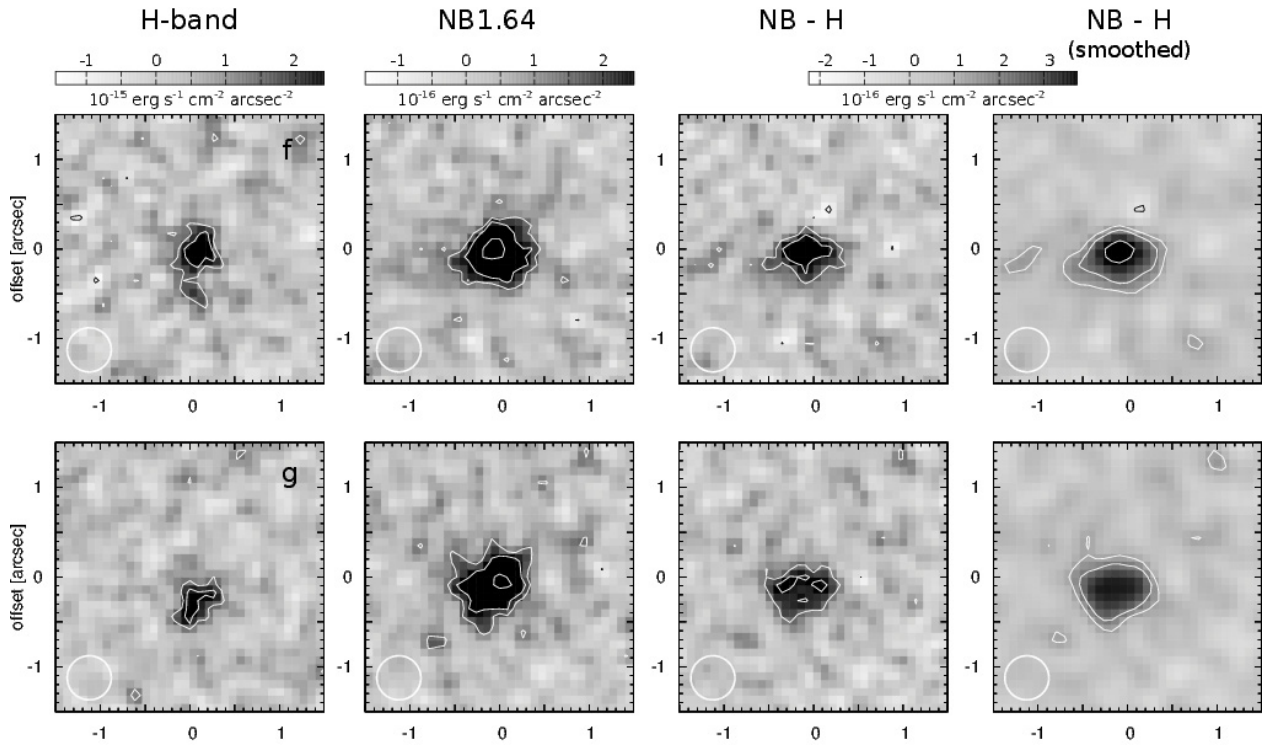

Fig. A.1. continued.